

# Dynamics of Dusty Radiation Pressure Driven Shells and Clouds: Fast Outflows from Galaxies, Star Clusters, Massive Stars, & AGN

Todd A. Thompson<sup>1</sup>, Andrew C. Fabian<sup>2</sup>, Eliot Quataert<sup>3</sup>, and Norman Murray<sup>4,5</sup>

<sup>1</sup>*Department of Astronomy and Center for Cosmology & Astro-Particle Physics, The Ohio State University, Columbus, Ohio 43210*

<sup>2</sup>*Institute of Astronomy, Madingley Road, Cambridge CB3 0HA*

<sup>3</sup>*Department of Astronomy and Theoretical Astrophysics Center, University of California, Berkeley, CA 94720-3411*

<sup>4</sup>*Canadian Research Chair in Astrophysics*

<sup>5</sup>*Canadian Institute for Theoretical Astrophysics, The University of Toronto, 60 St. George Street, Toronto Ontario M5S 3H8*

6 February 2015

## ABSTRACT

It is typically assumed that radiation pressure driven winds are accelerated to an asymptotic velocity of  $v_\infty \simeq v_{\text{esc}}$ , where  $v_{\text{esc}}$  is the escape velocity from the central source. We note that this is not the case for dusty shells and clouds. Instead, if the shell or cloud is initially optically-thick to the UV emission from the source of luminosity  $L$ , then there is a significant boost in  $v_\infty$  that reflects the integral of the momentum absorbed as it is accelerated. For shells reaching a generalized Eddington limit, we show that  $v_\infty \simeq (4R_{\text{UV}}L/M_{\text{sh}}c)^{1/2}$ , in both point-mass and isothermal-sphere potentials, where  $R_{\text{UV}}$  is the radius where the shell becomes optically-thin to UV photons, and  $M_{\text{sh}}$  is the mass of the shell. The asymptotic velocity significantly exceeds  $v_{\text{esc}}$  for typical parameters, and can explain the  $\sim 1000 - 2000 \text{ km s}^{-1}$  outflows observed from rapidly star-forming galaxies and active galactic nuclei if the surrounding halo has low gas density. Similarly fast outflows from massive stars can be accelerated on  $\sim \text{few} - 10^3 \text{ yr}$  timescales. These results carry over to clouds that subtend only a small fraction of the solid angle from the source of radiation and that expand as a consequence of their internal sound speed. We further consider the dynamics of shells that sweep up a dense circumstellar or circumgalactic medium. We calculate the “momentum ratio”  $\dot{M}v/(L/c)$  in the shell limit and show that it can only significantly exceed  $\sim 2$  if the effective optical depth of the shell to re-radiated FIR photons is much larger than unity. We discuss simple prescriptions for the properties of galactic outflows for use in large-scale cosmological simulations. We also briefly discuss applications to the dusty ejection episodes of massive stars, the disruption of giant molecular clouds, and AGN.

**Key words:** galaxies: formation, evolution, starburst — galaxies: star clusters: general

## 1 INTRODUCTION

In the galactic context, radiation pressure on dust grains has been discussed as a mechanism for launching galactic-scale winds in starbursts and rapidly star-forming galaxies (Harwit 1962; Chiao & Wickramasinghe 1972; Ferrara et al. 1990; Murray et al. 2005, 2011; Hopkins et al. 2012; Krumholz & Thompson 2013; Davis et al. 2014), in disrupting the dusty gas in individual star clusters (Harwit 1962; O’dell et al. 1967; Scoville et al. 2001; Krumholz & Matzner 2009; Murray et al. 2010), in launching fast outflows from AGN (Scoville & Norman 1995; Roth et al. 2012), in setting the  $M - \sigma$  relation (Fabian 1999; Murray et al. 2005), and in supporting starbursts and AGN disks against their own self-gravity (Ferrara 1993; Scoville 2003; Thompson et al. 2005; Andrews & Thompson 2011; Krumholz & Thompson 2012). Radiation pressure and momentum injection by supernovae and stellar winds plays an important role in models

of feedback in star-forming galaxies (Thompson et al. 2005; Hopkins et al. 2011; Ostriker & Shetty 2011; Hopkins et al. 2012; Faucher-Giguère et al. 2013).

In the stellar context, dusty shells are produced during the eruptions of supernova impostors and luminous blue variables, including  $\eta$ -Carinae (Davidson & Humphreys 1997; Smith & Gehrz 1998; Smith et al. 2003; Smith 2005, 2013), ultra-bright supernovae such as SN 2006gy (Miller et al. 2010), and SN 2008S-like transients (Kochanek 2011b; Kochanek et al. 2012; Prieto et al. 2008; Thompson et al. 2009; Prieto et al. 2009; Bond et al. 2009). Dusty shell formation and dynamics are also important to the phenomenology of R Coronae Borealis stars (e.g., Gillett et al. 1986), and continuous dusty winds are also produced generically by AGB stars (Ivezic & Elitzur 1995, 1997) and OH-IR stars and cool hypergiants like IRC+10420 (e.g., Ridgway et al. 1986; Humphreys et al. 1997).

The dynamics of radiation pressure-driven shells and clouds has been treated by a number of authors. Here, we provide a brief discussion that makes clearer the asymptotic velocity and momentum of an initially optically-thick shell or cloud and connect with observations in several contexts, but with a focus on rapidly star-forming galaxies. In particular, we critically examine the assumption that the asymptotic velocity of a radiation pressure driven shell or cloud is of order the escape velocity from the central body. This expectation follows from consideration of the momentum equation for a continuous time-steady radiation pressure driven flow with constant opacity from a point mass  $M$  and luminosity  $L$  (e.g., eq. 9 of Salpeter 1974):

$$v \frac{dv}{dr} = -\frac{GM}{r^2} + \frac{\kappa L}{4\pi r^2 c} \implies v_\infty^2 = v_{\text{esc}}^2(R_0) (\Gamma - 1), \quad (1)$$

where  $R_0$  is the initial radius,  $\Gamma = L/L_{\text{Edd}} = L/(4\pi GMc/\kappa)$ , and where the initial velocity of the medium has been neglected. For line-driven winds from hot sources (e.g., main sequence O stars, Wolf-Rayet stars, the central sources of planetary nebulae, AGN) the opacity is dominated by a forest of Doppler-shifted metal lines,  $R_0$  is typically of order the radius of the illuminating object, and the effective opacity is usually a multiplicative factor times  $\kappa_T$ , yielding the observed correlation between  $v_{\text{esc}}$  and  $v_\infty$  for some object classes (e.g., hot star winds; Abbott 1978). For continuous winds from AGB stars,  $R_0$  corresponds to the dust sublimation/formation radius ( $R_{\text{sub}}$ ; here the flow becomes super-Eddington) and  $\kappa$  is the flux-mean dust opacity as a function of radius (Ivezic & Elitzur 1995, 1997). For dusty flows that are optically-thick to the emission from the central star, most of the momentum is absorbed in a narrow layer near  $R_{\text{sub}}$ , wind material at larger radii is shielded from the central source, and  $v_\infty \simeq v_{\text{esc}}(R_{\text{sub}})\Gamma^{1/2}$ .

As we discuss in more detail below, the dynamics of a single geometrically thin dusty shell or cloud is different because as it expands it goes through an extended phase where it is optically-thick to the assumed incoming UV photons from the source, but optically-thin to the re-radiated IR emission from the grains. For a shell that subtends  $4\pi$  in this so-called single scattering limit (see eq. 19, below),

$$M_{\text{sh}} v \frac{dv}{dr} = -\frac{GMM_{\text{sh}}}{r^2} + \frac{L}{c} \implies v_\infty^2 \sim \frac{R_{\text{UV}}L}{M_{\text{sh}}c}, \quad (2)$$

where  $M_{\text{sh}}$  is the mass of the shell,  $R_{\text{UV}}$  is the radius at which the shell becomes optically-thin to the UV radiation, and we have assumed  $R_{\text{UV}} \gg R_0$  and that  $L/c \gg GMM_{\text{sh}}/R_0^2$ . The lack of radial dependence to the radiation pressure driving term shifts the momentum deposition to large scales,  $\sim R_{\text{UV}}$ , instead of  $R_0$  as in equation (1). Because the shell sees the entire source luminosity  $L$  during its entire evolution, it reaches high velocity.

Equations (1) and (2) are not as different as they first appear. Both expressions can be written as

$$v_\infty \sim v_{\text{esc}} \Gamma^{1/2} \quad (3)$$

in the limit that  $L \gg 4\pi GMc/\kappa$  and  $L \gg GMM_{\text{sh}}c/R_0^2$ , respectively. But, whereas in the case of a continuous flow the right hand side of equation (3) is evaluated at  $R_0$ , yielding the result of equation (1), in the case of a shell the right hand side is evaluated at  $R_{\text{UV}}$ , yielding equation (2). Another way to put the difference is that equation (1) implies the gas is accelerated in its first dynamical time at  $r \sim R_0$ , whereas equation (2) says that the “last” dynamical

time at  $R_{\text{UV}}$  dominates the shell’s acceleration and asymptotic velocity.

Equation (2) also applies in the case of an optically-thick cloud that subtends a fraction of the solid angle from the source, with the modification that  $L/c \rightarrow (L/c)(\pi R_c^2/4\pi r^2)$ , where  $R_c$  is the cloud radius. In the special case  $R_c \propto r$ , which in general does not obtain, the dynamics of shells maps trivially to clouds because the cloud solid angle is constant. However, even in the simplest case of a cloud expanding into vacuum, a new timescale enters the problem, the cloud expansion timescale  $t_{\text{exp}} \sim (d \ln R_c / dt)^{-1} = R_c/c_s$ , where  $c_s$  is the internal cloud sound speed and  $R_c$  is not a power-law in radius. This makes the dynamics of clouds somewhat more complicated than shells since the expansion rate of a cloud and hence the time evolution of its column density is uncoupled from its radial evolution away from the source. The latter is not true for a shell where the radius of the shell is directly coupled to its column density.

In the case of shells, an analogous point, but without the associated dust physics, is made in King (2003, 2005) for the case of shells driven by an AGN wind and by Dijkstra & Loeb (2008, 2009) in the case of  $\text{Ly}\alpha$  scattering. The case of dusty cloud dynamics in radiation pressure driven galactic winds has been discussed by Murray et al. (2005, 2011).

In this paper, we explore the acceleration of dusty shells and clouds in more detail and apply it to several physical systems. A shell geometry is motivated in some cases by observation of shells in the massive star and GMC contexts, by detached blue-shifted absorption line profiles in the case of some rapidly star-forming galaxies and AGN, and by theoretical arguments and modeling (e.g., Yeh & Matzner 2012). The key point is that dusty shell-like and cloudy outflows can attain significantly higher velocity than one might guess from an incorrect application of equation (1) as a result of the long phase of acceleration in the single-scattering limit (eq. 2). This issue is of particular importance in the extended gravitational potential wells of galaxies since the velocity attained near the source is crucial in determining whether or not it will escape to the scale of the virial radius, or, if it falls back, on what timescale. We are particularly motivated by the recent discoveries of very fast outflows from post-starburst galaxies by Tremonti et al. (2007) and Diamond-Stanic et al. (2012) (see also Sell et al. 2014; Geach et al. 2014).

In Section 2 we first consider the dynamics of a shell surrounding a point mass, and then treat extended mass distributions, as is more appropriate for the dynamics in a galactic gravitational potential. In Section 3 we provide a discussion of our results, including a discussion of fast outflows from galaxies and AGN, the total asymptotic momentum of radiation pressure accelerated shells and clouds, including the momentum ratio  $\dot{M}v_\infty/(L/c)$  in the shell limit, and we provide simple prescriptions for cosmological simulations that captures the expulsion of gas from rapidly star-forming galaxies. The extension to clouds is treated in Section 2.4. Our treatment is not as extensive as for shells because the dynamics of a given cloud in an outflow depends on many parameters including the ensemble of clouds between a given cloud and the radiation sources, the cloud’s internal sound speed and its evolution, the pressure of the background medium, which determines a cloud’s expansion/thermal history, and destruction processes such as the Kelvin-Helmholtz instability and evaporation. Nevertheless, we discuss the dynamics of individual clouds in the context of our results for the case of shells and show that our primary conclusion — that fast

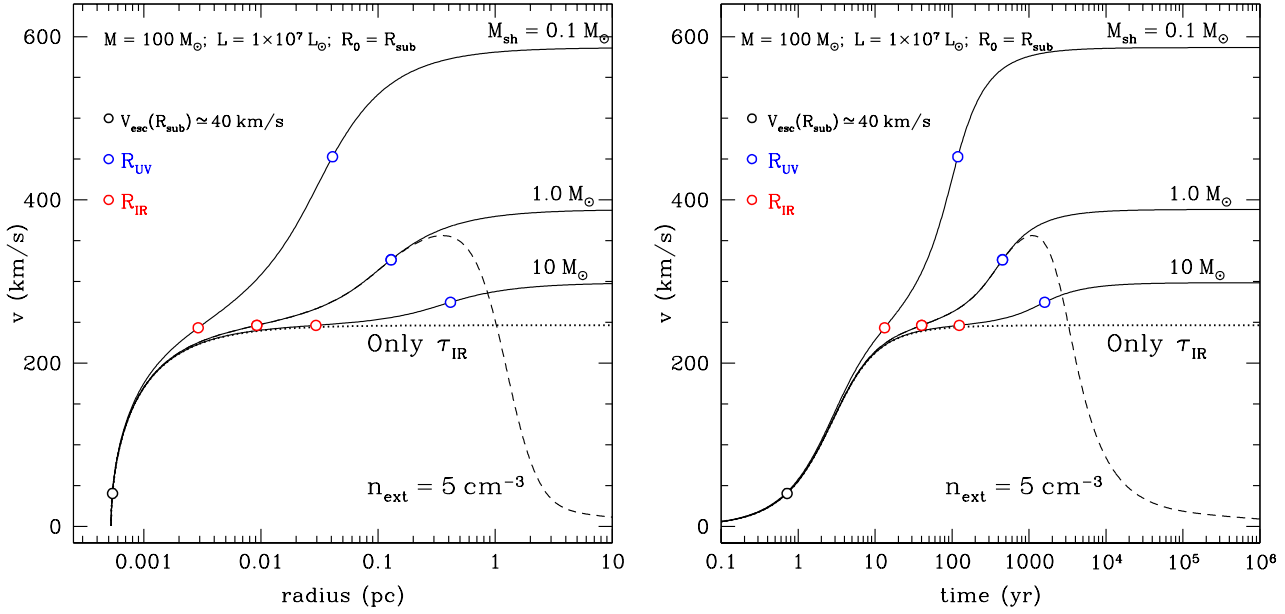


**Figure 1.** Velocity as a function of radius (left panel) and time (right panel) for dusty shells with mass 10, 1, and  $0.1 M_{\odot}$  ejected from a massive star with  $M = 100 M_{\odot}$  and  $L = 10^7 L_{\odot}$  (solid lines; eq. 6). The dotted line shows the evolution if *only* the  $\tau_{\text{IR}}$  term is included in equation (6). The dashed line shows the dynamics of the  $1 M_{\odot}$  shell with a constant density external medium of  $n_{\text{ext}} = 5 \text{ cm}^{-3}$  (see Section 2.3; eq. 35). The black, red, and blue circles denote  $v_{\text{esc}}$ ,  $R_{\text{IR}}$ , and  $R_{\text{UV}}$  (eqs. 5, 6), respectively. All shells have  $R_0 = R_{\text{sub}}$ , the dust sublimation radius, where dust first forms (see text).

outflows with  $v_{\infty}$  significantly larger than  $v_{\text{esc}}(R_0)$  are generically obtained — carries over.

## 2 DYNAMICS OF SHELLS DRIVEN BY RADIATION PRESSURE

### 2.1 Point Mass

Assume a point source with UV luminosity  $L$  and total mass  $M$ , surrounded by a dusty gas shell of mass  $M_{\text{sh}}$  an initial distance  $R_0$  from the central source. We define two characteristic radii:

$$R_{\text{IR}} = (\kappa_{\text{IR}} M_{\text{sh}}/4\pi)^{1/2} \simeq 0.3 \text{ kpc } \kappa_{\text{IR},0.7}^{1/2} M_{g,9}^{1/2} \quad (4)$$

$$R_{\text{IR}} = (\kappa_{\text{IR}} M_{\text{sh}}/4\pi)^{1/2} \simeq 1.9 \times 10^3 \text{ AU } \kappa_{\text{IR},0.7}^{1/2} M_{g,0}^{1/2}$$

is where the shell becomes optically-thin to the re-radiated IR, and

$$R_{\text{UV}} = (\kappa_{\text{UV}} M_{\text{sh}}/4\pi)^{1/2} \simeq 4 \text{ kpc } \kappa_{\text{UV},3}^{1/2} M_{g,9}^{1/2} \quad (5)$$

$$R_{\text{UV}} = (\kappa_{\text{UV}} M_{\text{sh}}/4\pi)^{1/2} \simeq 4.6 \times 10^4 \text{ AU } \kappa_{\text{UV},3}^{1/2} M_{g,0}^{1/2}$$

is where the shell becomes optically-thin to the UV radiation from the source. In the above,  $M_{\text{sh},x} = M_{\text{sh}}/10^x M_{\odot}$ , we have scaled for both the galaxy and stellar contexts,  $\kappa_{\text{UV},3} = \kappa_{\text{UV}}/10^3 f_{\text{dg,MW}} \text{ cm}^2 \text{ g}^{-1}$  of gas, where  $f_{\text{dg,MW}}$  is the dust-to-gas ratio scaled to the Milky Way value. and  $\kappa_{\text{IR},0.7} = \kappa_{\text{IR}}/10^{0.7} f_{\text{dg,MW}} \text{ cm}^2 \text{ g}^{-1}$  roughly approximates the Rosseland-mean dust opacity over a range of temperatures from  $\sim 100 - 1000 \text{ K}$ .

The general expression for momentum conservation for a thin shell of mass  $M_{\text{sh}}$ , approximately valid in the limits of both small

and large UV and IR optical depth is

$$\frac{d}{dt} (M_{\text{sh}} v) = -\frac{GM M_{\text{sh}}}{r^2} + (1 + \tau_{\text{IR}} - e^{-\tau_{\text{UV}}}) \frac{L}{c}, \quad (6)$$

where

$$\tau_{\text{IR,UV}} = \kappa_{\text{IR,UV}} M_{\text{sh}}/(4\pi r^2) \quad (7)$$

are the IR and UV optical depths of the shell and where we have assumed that the dust and gas are dynamically coupled. Note the three terms multiplying  $L/c$  in equation (6). The first term (“1”) is due to the direct radiation field. It represents the radiation pressure force exerted if each photon interacts just once with the dusty medium, is converted into an IR photon, and then escapes the system. The second term accounts for reprocessed radiation if the shell is optically-thick to the re-radiated IR emission. The third term goes to the appropriate limit when  $\tau_{\text{UV}} \ll 1$  ( $\tau_{\text{IR}} \ll 1$  also), canceling the “1” and yielding the familiar optically-thin radiation pressure force for a source dominated by UV emission ( $\kappa_{\text{UV}} L/4\pi r^2 c$ ).

Setting the acceleration in equation (6) equal to zero, we obtain the generalized Eddington limit for a shell starting at  $R_0$ :

$$L_{\text{Edd}} = \frac{GM M_{\text{sh}} c}{R_0^2} (1 + \tau_{\text{IR}} - e^{-\tau_{\text{UV}}})^{-1}, \quad (8)$$

where  $M$  and  $M_{\text{sh}}$  are understood to be the total mass interior to  $R_0$  and the shell mass at  $R_0$ , respectively. The Eddington ratio is then

$$\Gamma_{\text{tot}} = L/L_{\text{Edd}}. \quad (9)$$

There are three characteristic Eddington ratios, depending on the optical depth of the shell at  $R_0$ . If the shell is optically-thick to the IR ( $\tau_{\text{IR}}(R_0) > 1$ ), then the relevant Eddington ratio is

$$\Gamma_{\text{IR}} = L/(4\pi GM c/\kappa_{\text{IR}}). \quad (10)$$

If the shell is optically-thin to the IR, but optically-thick to the UV ( $\tau_{\text{IR}} < 1$ ,  $\tau_{\text{UV}} > 1$ ) at  $R_0$ , then the single-scattering Eddington ratio (the “1” in eqs. 6 and 9)

$$\Gamma_{\text{SS}} = L/(GM_{\text{sh}}c/R_0^2), \quad (11)$$

determines the dynamics. Finally, if the shell is optically-thin to the incident UV radiation ( $\tau_{\text{UV}} < 1$  at  $R_0$ ), then the relevant Eddington ratio is

$$\Gamma_{\text{UV}} = L/(4\pi GM_{\text{sh}}c/\kappa_{\text{UV}}). \quad (12)$$

Before solving equation (6) for specific example systems, we consider several simple analytic limits.

We first assume that the mass of the shell is constant as a function of radius (i.e., the shell expands into vacuum). Then, dropping the  $e^{-\tau_{\text{UV}}}$  term in equation (6) in the regime  $R_0 \leq r \leq R_{\text{UV}}$  ( $\tau_{\text{UV}} > 1$ ) and solving for the velocity at  $v_{\text{UV}} = v(R_{\text{UV}})$ , one finds that

$$v_{\text{UV}}^2 = v_0^2 + \frac{2GM}{R_0} \left( \Gamma_{\text{SS}} \frac{R_{\text{UV}}}{R_0} + \Gamma_{\text{IR}} - 1 \right) \left( 1 - \frac{R_0}{R_{\text{UV}}} \right), \quad (13)$$

where  $v_0 = v(R_0)$ . Once the shell reaches  $R_{\text{UV}}$  it becomes optically-thin to the incident UV photons, and the momentum equation for the shell in the regime  $R_{\text{UV}} \leq r \leq \infty$  is just

$$v \frac{dv}{dr} = -\frac{GM}{r^2} + \frac{\kappa_{\text{UV}} L}{4\pi r^2 c}. \quad (14)$$

Solving, and substituting from equation (13) one finds that

$$v_{\infty}^2 = v_0^2 + \frac{2GM}{R_0} \left[ \Gamma_{\text{SS}} \frac{R_{\text{UV}}}{R_0} + \Gamma_{\text{IR}} - 1 \right] \left( 1 - \frac{R_0}{R_{\text{UV}}} \right) + \frac{GM}{R_{\text{UV}}} (\Gamma_{\text{UV}} - 1) \quad (15)$$

which can be rewritten as

$$v_{\infty}^2 = v_0^2 + \frac{2GM}{R_0} \left[ 2\Gamma_{\text{SS}} \frac{R_{\text{UV}}}{R_0} \left( 1 - \frac{R_0}{2R_{\text{UV}}} \right) + \Gamma_{\text{IR}} \left( 1 - \frac{R_0}{R_{\text{UV}}} \right) - 1 \right] \quad (16)$$

These expressions are important. The ratio  $R_{\text{UV}}/R_0$  can be much larger than unity and thus, even if the initial Eddington ratio of the flow is equal to unity  $\Gamma_{\text{tot}} \simeq 1$  at  $R_0$ , the shell can still be accelerated to  $v_{\infty} \gg v_{\text{esc}}$  if it starts with  $\tau_{\text{UV}} > 1$ . Taking  $R_0 \ll R_{\text{UV}}$ , note that the ratio of the first two terms in square brackets in equation (16) is

$$\left( 2\Gamma_{\text{SS}} \frac{R_{\text{UV}}}{R_0} \right) \frac{1}{\Gamma_{\text{IR}}} = \frac{2}{\tau_{\text{IR}}(R_0)^{1/2}} \left( \frac{\kappa_{\text{UV}}}{\kappa_{\text{IR}}} \right)^{1/2}, \quad (17)$$

and thus the  $\Gamma_{\text{SS}}$  term dominates unless  $\tau_{\text{IR}}(R_0) > 4\kappa_{\text{UV}}/\kappa_{\text{IR}} \sim 10^3$ . Thus, assuming  $\Gamma_{\text{IR}} \ll 2\Gamma_{\text{SS}} R_{\text{UV}}/R_0$  and then taking  $v_0 \sim 0$ ,  $R_0 \ll R_{\text{UV}}$  in equation (16), one finds that

$$v_{\infty} \simeq v_{\text{esc}} \left( 2\Gamma_{\text{SS}} \frac{R_{\text{UV}}}{R_0} \right)^{1/2} = v_{\text{esc}} \Gamma_{\text{SS}}^{1/2} [4\tau_{\text{UV}0}]^{1/4}, \quad (18)$$

where  $v_{\text{esc}}$  is understood to be the escape velocity from the launch radius  $R_0$  in a point-mass potential, and  $\tau_{\text{UV}0} = \tau_{\text{UV}}(R_0)$  is the UV optical depth at  $R_0$ . This expression can be rewritten in terms

of the luminosity ( $L_x = L/10^x L_{\odot}$ ) as<sup>1</sup>

$$\begin{aligned} v_{\infty} &\simeq \left( \frac{4R_{\text{UV}}L}{M_{\text{sh}}c} \right)^{1/2} \simeq \left( \frac{2L}{c} \right)^{1/2} \left( \frac{\kappa_{\text{UV}}}{\pi M_{\text{sh}}} \right)^{1/4} \\ &\simeq 320 \text{ km s}^{-1} L_7^{1/2} \kappa_{\text{UV},3}^{1/4} M_{\text{sh},0}^{-1/4}, \\ &\simeq 1800 \text{ km s}^{-1} L_{13}^{1/2} \kappa_{\text{UV},3}^{1/4} M_{\text{sh},9}^{-1/4}. \end{aligned} \quad (19)$$

As discussed in Section 1, equation (16), and the simple results given in equations (18) and (19) for the asymptotic velocity of a radiation pressure driven shell are qualitatively and quantitatively different from the expectation that  $v_{\infty} \simeq v_{\text{esc}}(R_0)(\Gamma_{\text{tot}} - 1)^{1/2}$  (eq. 1). In particular, from equation (18) one sees that  $v_{\infty}$  can significantly exceed  $v_{\text{esc}}(R_0)$ , even for an Eddington ratio near unity at  $R_0$ : high Eddington ratios are not required for high velocities with respect to the escape velocity. Instead, the initial value of the UV optical depth through the shell determines its dynamical evolution. The typical “boost” in the asymptotic velocity compared to  $v_{\text{esc}}(R_0)$  is

$$\begin{aligned} \Gamma_{\text{SS}}^{1/2} [4\tau_{\text{UV}0}]^{1/4} &\simeq 9 \Gamma_{\text{SS}}^{1/2} R_{0,0.1 \text{ kpc}}^{-1/2} \kappa_3^{1/4} M_{g,9}^{1/4} \\ &\simeq 73 \Gamma_{\text{SS}}^{1/2} R_{0,10 \text{ AU}}^{-1/2} \kappa_3^{1/4} M_{g,0}^{1/4} \end{aligned} \quad (20)$$

Thus, in the context of galactic winds, even if  $\Gamma_{\text{SS}} \sim 1$ , one expects the asymptotic velocity of the shell to exceed the escape velocity from the launch region by nearly an order of magnitude (see Sections 2.2 and 2.3 for a discussion of extended galactic potentials). In the stellar context, the boost may be larger. The physics of this enhancement in the asymptotic velocity comes simply from the radial dependence of the single-scattering radiation pressure term; in particular, aside from acting only until  $r \simeq R_{\text{UV}}$  it has no radial fall-off, whereas both the gravitational acceleration and the flux drop with radius as  $r^{-2}$ . The result that  $v_{\infty}^2/R_{\text{UV}} \sim L/M_{\text{sh}}c$  is precisely what one would then get from dimensional analysis of equation (6), which is equivalent to the result  $v_{\infty} \sim v_{\text{esc}}\Gamma^{1/2}$ , but evaluated at  $R_{\text{UV}}$  (see discussion after eq. 2).

As an aside, note that the dynamical stability of a dusty shell to radial perturbations is different depending on whether or not the radiation pressure force is  $f_{\text{rad}} = \kappa L/4\pi r^2 c$  or  $L/M_{\text{sh}}c$ . In the latter, single-scattering limit, shells are unstable to radial perturbations since  $f_{\text{rad}} \propto r^0$ , whereas the gravitational force is  $f_{\text{grav}} \propto r^{-2}$ . Thus, if an equilibrium is established with  $\Gamma_{\text{SS}} = 1$  small perturbations would drive the shell to smaller  $r$  causing collapse, or larger  $r$ , causing dynamical escape with  $v_{\infty}$  given by equation (19), different from the behavior if  $f_{\text{rad}} \propto r^{-2}$ .

Figure 1 shows integrations of equation (6) for a massive star outburst (left panel). Shells of 0.1, 1, and 10  $M_{\odot}$  are accelerated from the dust sublimation radius  $R_{\text{sub}} = (L/16\pi\sigma_{\text{sb}}T_{\text{sub}}^4)^{1/2}$ , where  $T_{\text{sub}} \simeq 1500 \text{ K}$  to pc scales for an outburst from a massive star with  $M = 100 M_{\odot}$  and luminosity  $10^7 L_{\odot}$ . The solid lines show the full solution to equation (6), whereas the dotted line shows the solution with *only* the  $\tau_{\text{IR}}$  term. The dashed line, which shows the change in dynamics when the 1  $M_{\odot}$  shell interacts with a constant density medium, is discussed in Section 2.3. The black, red, and blue dots mark the radial location of  $v_{\text{esc}}(R_{\text{sub}})$ ,  $\Gamma_{\text{IR}}$  and  $R_{\text{UV}}$  respectively. The initial IR optical depths of the shells are

<sup>1</sup> Note that these expressions are only applicable when  $R_0 \ll R_{\text{UV}}$ . As the mass of the shell becomes small and  $\tau_{\text{UV}}(R_0)$  becomes less than unity,  $v_{\infty} = v_{\text{esc}}(R_0)(\Gamma_{\text{UV}}(R_0) - 1)^{1/2}$  (see eq. 49).



$\simeq 30, 300$ , and  $3000$ , and  $\Gamma_{\text{SS}} \simeq 1, 0.1$ , and  $0.01$ , respectively (see 3.7). For all shells,  $\Gamma_{\text{IR}} \simeq 40$ .

Based on the fact that the initial IR optical depth is larger than unity at  $R_0 = R_{\text{sub}} (\simeq 100 \text{ AU})$  and that  $\Gamma_{\text{IR}} \gg \Gamma_{\text{SS}}$ , one might have expected that  $v_\infty \simeq v_{\text{esc}}(R_{\text{sub}}) (\Gamma_{\text{IR}} - 1)^{1/2} \simeq 250 \text{ km s}^{-1}$ , as shown by the dotted line, which only includes the  $\tau_{\text{IR}}$  term in equation (6). Instead, the single-scattering term in equation (6) dominates the dynamics on large scales, accelerating the shells to velocities much larger than  $v_{\text{esc}}(R_{\text{sub}}) \simeq 40 \text{ km s}^{-1}$  since  $R_{\text{UV}}/R_0 \gg 1$ .

If we were to instead drop the  $\tau_{\text{IR}}$  term from our solution of equation (6) for the shells in Figure 1, the initial rapid rise in velocity to  $\simeq 250 \text{ km/s}$  is missing for the  $0.1 M_\odot$  shell, but its subsequent dynamics is similar to that shown because  $\Gamma_{\text{SS}}$  is just larger than unity at  $R_0$ . For the other more massive shells,  $\Gamma_{\text{SS}}$  is less than unity at  $R_0$  and they fall back toward the central star, even though on larger scales in the full solution shown in Figure 1 this term is responsible for substantial acceleration. Finally, if we were to assume incorrectly that the shells were optically-thin to the UV at  $R_0$ , so that the radiation pressure term on the right hand side of equation (6) was just  $\tau_{\text{UV}} L/c$ , the shells would be accelerated rapidly to  $v_{\text{esc}}(R_0) \Gamma_{\text{UV}}^{1/2} \sim 3600 \text{ km/s}$ . These various limits of the momentum equation are useful in considering the dynamics of rapidly expanding clouds discussed in Section 2.4.

Turning back to the solid lines in Figure 1, one might have also expected that the shell with the highest mass and highest initial optical depth to have the highest asymptotic velocity, but because these results are shown for fixed luminosity, and because  $\Gamma_{\text{SS}} \propto M_{\text{sh}}^{-1}$ , one has that  $v_\infty \propto M_{\text{sh}}^{-1/4}$  (eq. 19). Thus, low mass shells are driven to higher asymptotic velocity than higher mass shells at fixed  $L$ ; for  $M_{\text{sh}} = 0.01 M_\odot$  (not shown),  $v_\infty \simeq 970 \text{ km s}^{-1}$ . More discussion of these types of eruptions are included in Section 3.6. Since such outbursts have high initial IR optical depths, their dynamics may be important in assessing multi-dimensional instabilities that may limit the momentum coupling between the radiation field and the shell as it is accelerated (see 3.7).<sup>2</sup>

Finally, note that the characteristic acceleration timescale  $t_{\text{acc}} \sim v_\infty / (dv/dt)$  is long on the scale of observations of a single massive star outburst:

$$\begin{aligned} t_{\text{acc}} &\sim \left(\frac{2c}{L}\right)^{1/2} \left(\frac{\kappa_{\text{UV}}}{4\pi}\right)^{1/4} M_{\text{sh}}^{3/4} \\ &\sim 1100 \text{ yr } L_7^{-1/2} M_{\text{sh},0}^{3/4} \kappa_{\text{UV},3}^{1/4} \\ &\sim 6.4 \times 10^6 \text{ yr } L_{13}^{-1/2} M_{\text{sh},9}^{3/4} \kappa_{\text{UV},3}^{1/4}. \end{aligned} \quad (21)$$

The scaling for the massive star outburst agrees with the calcula-

<sup>2</sup> Note that throughout this work we assume that  $Lt/(M_{\text{sh}} v^2/2) \gg 1$ . For high enough IR optical depths it is possible for the radiation field to do sufficient work on the matter to enter the “photon tiring” regime discussed by Owocki & Gayley (1997) and Owocki et al. (2004) in the context of line-driven winds. Examining  $Lt/(M_{\text{sh}} v^2/2)$  as a function of radius for the models in Figure 1, we find that it is always larger than unity, although it becomes as low as  $\sim 2$  on scales smaller than the  $\tau_{\text{IR}} = 1$  point (red circle) for the model with  $M_{\text{sh}} = 10 M_\odot$ . An estimate of the critical shell mass such that  $Lt/(M_{\text{sh}} v^2/2) = 1$  and photon tiring becomes important is  $M_{\text{sh,tiring}} = L^{3/4} c^{3/2} \pi^{1/4} / (2^{3/2} \sigma_{\text{SB}}^{5/4} T_{\text{sub}}^5 \kappa_{\text{IR}}^{3/2})$ , obtained by taking  $\tau_{\text{IR}}(R_{\text{sub}}) = 2c/v_\infty$  in the limit that  $\Gamma_{\text{IR}} \gg 1$  at  $R_{\text{sub}}$ . For the parameters of Figure 1 this is  $M_{\text{sh,tiring}} \simeq 8 M_\odot L_7^{3/4} T_{1500}^{-5} \kappa_{\text{IR},0.7}^{-3/2}$ . Note the strong dependencies.

tions shown in Figure 1 and implies that high-velocity shells driven by this physics will be associated with many old outbursts.

## 2.2 Extended Mass Distributions with Fixed Shell Mass

In the context of outflows driven from galaxies, it is important to consider the extended stellar and dark matter potentials. For illustration we assume that the total mass distribution is an isothermal sphere:  $M(r) = 2\sigma^2 r/G$ , where  $\sigma$  is the velocity dispersion. Assuming momentarily that the mass of the shell is constant, we then have that

$$M_{\text{sh}} v \frac{dv}{dr} = -\frac{2\sigma^2}{r} + (1 + \tau_{\text{IR}} - e^{-\tau_{\text{UV}}}) \frac{L}{c}. \quad (22)$$

and

$$L_{\text{Edd}} = \frac{2\sigma^2 M_{\text{sh}} c}{R_0} (1 + \tau_{\text{IR}} - e^{-\tau_{\text{UV}}})^{-1}. \quad (23)$$

We again define

$$\Gamma_{\text{tot}} = L/L_{\text{Edd}}, \quad (24)$$

and the three characteristic Eddington ratios

$$\Gamma_{\text{IR,UV}} = L/(8\pi\sigma^2 R_0 c/\kappa_{\text{IR,UV}}) \quad (25)$$

and

$$\Gamma_{\text{SS}} = L/(2\sigma^2 M_{\text{sh}} c/R_0). \quad (26)$$

Again taking  $e^{-\tau_{\text{UV}}} \sim 0$  in the regime  $R_0 \leq r \leq R_{\text{UV}}$ , we find that

$$\begin{aligned} v_{\text{UV}}^2 &= v_0^2 + 4\sigma^2 \left[ \left( \Gamma_{\text{SS}} \frac{R_{\text{UV}}}{R_0} + \Gamma_{\text{IR}} \right) \left( 1 - \frac{R_0}{R_{\text{UV}}} \right) \right. \\ &\quad \left. - \ln \left( \frac{R_{\text{UV}}}{R_0} \right) \right], \end{aligned} \quad (27)$$

and then integrating to an outer radius  $R_{\text{out}}$  where the approximation of an isothermal potential breaks down,

$$\begin{aligned} v_{\text{out}}^2 &= v_0^2 + 4\sigma^2 \left[ 2\Gamma_{\text{SS}} \frac{R_{\text{UV}}}{R_0} \left( 1 - \frac{R_0}{R_{\text{UV}}} - \frac{R_{\text{UV}}}{2R_{\text{out}}} \right) \right. \\ &\quad \left. + \Gamma_{\text{IR}} \left( 1 - \frac{R_0}{R_{\text{UV}}} \right) - \ln \left( \frac{R_{\text{out}}}{R_0} \right) \right]. \end{aligned} \quad (28)$$

The same factor that appears in the point-mass limit —  $(2\Gamma_{\text{SS}} R_{\text{UV}}/R_0)^{1/2}$  — which can boost the asymptotic velocity far above  $v_{\text{esc}}(R_0)$  (eq. 19) also appears in the limit of an extended mass distribution. Assuming that  $\Gamma_{\text{tot}} \geq 1$ ,  $R_0 \ll R_{\text{UV}}$ ,  $R_{\text{UV}} \ll R_{\text{out}}$ , and that  $\Gamma_{\text{IR}} \ll 2\Gamma_{\text{SS}} R_{\text{UV}}/R_0$ , one finds that

$$\begin{aligned} v_{\text{out}} &\simeq 2\sigma \Gamma_{\text{SS}}^{1/2} [4\tau_{\text{UV},0}]^{1/4} \\ &\simeq 18\sigma \Gamma_{\text{SS}}^{1/2} R_{0,0.1 \text{ kpc}}^{-1/2} \kappa_{\text{UV},3}^{1/4} M_{9,9}^{1/4} \end{aligned} \quad (29)$$

fully analogous with equation (19) in the point-mass limit. If we define  $f_{\text{sh}}$  as the fraction of mass within the launch radius  $R_0$  that goes into the shell,

$$M_{\text{sh}} = f_{\text{sh}} \frac{2\sigma^2 R_0}{G}, \quad (30)$$

we find that

$$\begin{aligned} v_{\text{out}} &\simeq 2\Gamma_{\text{SS}}^{1/2} \left( \frac{2\kappa_{\text{UV}} \sigma^6 f_{\text{sh}}}{\pi R_0 G} \right)^{1/4} \\ &\simeq 4 \times 10^3 \text{ km s}^{-1} \Gamma_{\text{SS}}^{1/2} \kappa_{\text{UV},3}^{1/4} f_{\text{sh}}^{1/4} R_{0,0.1 \text{ kpc}}^{-1/4}. \end{aligned} \quad (31)$$

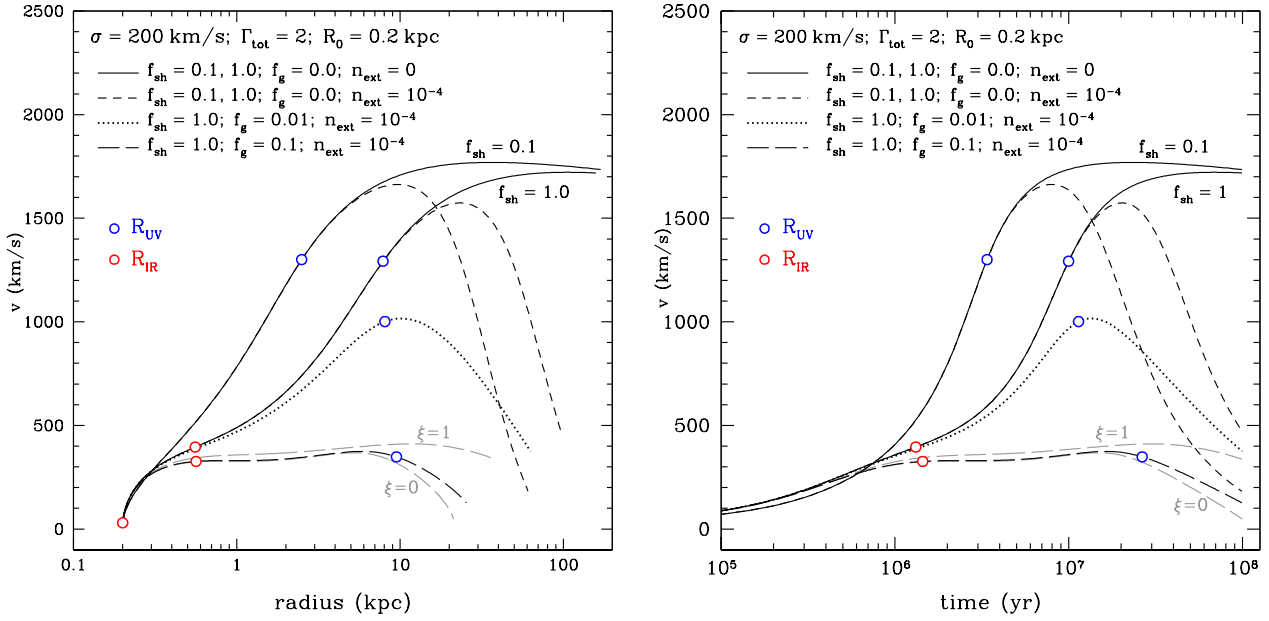


**Figure 2.** Velocity as a function of radius (left panel) and time (right panel) for dusty shells in an isothermal potential with  $\sigma = 200 \text{ km s}^{-1}$ , starting from a launch radius of  $R_0 = 0.2 \text{ kpc}$  and  $\Gamma_{\text{tot}} = 2$  (eqs. 8 & 9). The two solid lines show the evolution for a freely expanding shell with no external medium ( $f_g = 0$ ,  $n_{\text{ext}} = 0 \text{ cm}^{-3}$ ) and with  $f_{\text{sh}} = 0.1$ , and  $1$ , where  $f_{\text{sh}}$  is defined by equation (30), so that  $M_{\text{sh}} \simeq 3.7 \times 10^8 M_{\odot}$  and  $\simeq 3.7 \times 10^9 M_{\odot}$ , respectively. Given  $\Gamma_{\text{tot}}$ , the total luminosities are  $\simeq 8.9 \times 10^{12} L_{\odot}$  and  $\simeq 2.6 \times 10^{13} L_{\odot}$  for  $f_{\text{sh}} = 0.1$ , and  $1$ , respectively. The short dashed lines show the evolution of both shells if they interact with a constant density halo that has  $n_{\text{ext}} = 10^{-4} \text{ cm}^{-3}$  (see Section 2.3; eq. 35). The dotted and long dashed lines show the evolution of the  $f_{\text{sh}} = 1$  shell if we add an external gas density distribution that follows equation (32) with  $f_g = 0.01$  and  $0.1$ , respectively (see eq. 33). The dust content of the swept up gas in all cases is assumed equivalent to a fraction  $\xi = 0.1$  (see eq. 36) times the Milky Way value, except for the two gray long-dashed curves, which show the change in the dynamics for the  $f_{\text{sh}} = 1.0$ ,  $f_g = 0.1$ , and  $n_{\text{ext}} = 10^{-4} \text{ cm}^{-3}$  model if the external medium has zero dust ( $\xi = 0$ ) or a Milky Way value ( $\xi = 1$ ). The red, and blue circles denote  $R_{\text{IR}}$  and  $R_{\text{UV}}$  (eqs. 5, 6), respectively. See Fig. 4 for the momentum ratio  $\zeta$  (Section 3.1) and column density evolution of these models.

Note that these analytic estimates overestimate  $v_{\text{out}}$  because they ignore the logarithmic factor in equation (28).

Figure 2 shows the velocity evolution of massive dusty shells launched in an isothermal potential. We assume this potential extends to  $100 \text{ kpc}$  for simplicity, even though this approximation breaks down for real galaxies on the scale of  $\sim 10 \text{ s of kpc}$ . For massive shells (e.g.,  $f_{\text{sh}} = 1$ ), we include the self-gravity of the shell itself in the total mass  $M$  in our solution to the momentum equation (6) using  $M = M(< r) + M_{\text{sh}}/2$ . The two solid lines show velocity as a function of radius (left panel) and time (right panel) for  $f_{\text{sh}} = 0.1$  and  $f_{\text{sh}} = 1$  (see eq. 30), corresponding to  $M_{\text{sh}} = 3.7 \times 10^8$  and  $3.7 \times 10^9 M_{\odot}$ , respectively, launched from a galaxy with  $\sigma = 200 \text{ km s}^{-1}$ , and from a radius  $R_0 = 0.2 \text{ kpc}$ . For each shell, we assume  $\Gamma_{\text{tot}} = 2$ , so that  $L \simeq 8.9 \times 10^{12}$ ,  $2.6 \times 10^{13} L_{\odot}$  as might be provided by a central starburst and/or active galactic nucleus. These two models (solid lines) assume that the shell expands into vacuum. In Section 2.3 we calculate the dynamics of shells expanding into a constant density medium and a medium with an isothermal sphere density profile (dashed and dotted lines), and with a varying gas-to-dust ratio for the swept up medium (gray dashed lines). See Section 2.3.

For the parameters of the shells shown by the solid lines in Figure 2, the naive expectation in many models of galactic winds would have been that  $v_{\infty} \simeq 2\sigma(\Gamma_{\text{tot}} - 1)^{1/2} \simeq 400 \text{ km s}^{-1}$ . However, because of the factor  $(2\Gamma_{\text{SS}}R_{\text{UV}}/R_0)^{1/2}$  in equation (28) caused by long-term acceleration of the shell in the single-scattering limit, the actual velocities are  $\sim 4$  times this value,

reaching  $\sim 1600 \text{ km s}^{-1}$  on  $\sim 1 - 10 \text{ kpc}$  scales. These high velocities have important implications for observations (see Section 3).

### 2.3 Evolving Shells

In the general case of a massive shell driven into the circumgalactic medium of highly star-forming galaxies, we expect the shell to sweep up mass and the assumptions of the previous section break down. In the limiting case that the shell sweeps up less than its initial mass by the time it reaches  $R_{\text{UV}}$ , we expect the dynamics to be qualitatively similar. However, if the mass of the swept-up material approaches the initial mass of the shell on the scale of  $R_{\text{UV}}$ , we expect the shell dynamics to be altered. If we assume that the circumgalactic gas takes the form of a static isothermal sphere with gas density

$$\rho = \frac{f_g \sigma^2}{2\pi G r^2}, \quad (32)$$

the critical value for  $f_g$  such that the swept up gas mass  $M_{\text{sh}}(R_{\text{UV}})$  is equal to the initial shell mass  $M_{\text{sh}}(R_0)$  is

$$f_{g, \text{crit}} = \frac{G}{\sigma^2} \left( \frac{\pi M_{\text{sh}}(R_0)}{\kappa_{\text{UV}}} \right)^{1/2} \simeq 0.01 \sigma_{200}^{-2} M_{\text{sh}, 9}^{1/2} \kappa_{\text{UV}, 3}^{-1/2}. \quad (33)$$

Thus, for  $f_g \gtrsim f_{g, \text{crit}}$ , we expect the shell dynamics to be different from the solid lines shown in Figure 2. In particular, we expect the shell to decelerate, in accord with momentum conservation.

An analogous estimate can be made in the stellar case, where the shell from the eruption sweeps up the matter in a steady preceding stellar wind of mass loss rate  $\dot{M}$ . In this case, the density profile is an isothermal sphere with  $\rho = \dot{M}/(4\pi r^2 v_w)$ , where  $v_w$  is the wind velocity. Setting the total swept up mass  $\dot{M}(r - R_0)/v_w$  equal to the initial shell mass, one derives a critical mass loss rate such that the shell sweeps up its own mass on a scale  $R_{UV}$ :

$$\begin{aligned} \dot{M}_{\text{crit}} &= \left( \frac{4\pi M_{\text{sh}} v_w^2}{\kappa_{UV}} \right)^{1/2} \\ &\simeq 8 \times 10^{-4} M_{\odot} \text{ yr}^{-1} M_{\text{sh},0}^{1/2} \kappa_{UV,3}^{-1/2} v_{w,100}, \end{aligned} \quad (34)$$

where  $v_{w,100} = v_w/100 \text{ km s}^{-1}$ .

If we take the surrounding external medium to have constant density, we can estimate the critical density such that the swept up mass is equal to the initial shell mass at  $R_{UV}$ . This limit is applicable to massive stars in constant density circumstellar envelopes, or shells interacting with the surrounding ISM, and to shells driven from galaxies that sweep up matter from the hot near-constant density halo (e.g., Maller & Bullock 2004). The critical external density required to slow the shell on a scale  $R_{UV}$  is

$$\begin{aligned} n_{\text{ext,crit}} &= 4.5 \times 10^3 \text{ cm}^{-3} \kappa_{UV,3}^{-3/2} M_{\text{sh},0}^{1/2} \\ &= 0.1 \text{ cm}^{-3} \kappa_{UV,3}^{-3/2} M_{\text{sh},9}^{1/2}. \end{aligned} \quad (35)$$

The normalization for the massive star case in the first line is very large compared to what would be expected in the average region of a star-forming galaxy like the Milky Way (e.g.,  $\sim 1 \text{ cm}^{-3}$ ), and even larger than an average volume within most starburst galaxies (e.g., Krumholz & Thompson 2007). The normalization for the galaxy case in the second line is also large compared to the very large-scale approximately constant density hot component of the circumgalactic medium, which may have  $n \sim 10^{-3} - 10^{-4} \text{ cm}^{-3}$  (e.g., Maller & Bullock 2004). One might then expect that in both cases the constant density medium will not have an important effect on the shell dynamics. However, because the swept up mass scales with  $r^3$  in the constant density case we expect the shell to slow significantly on scales larger than  $R_{UV}$  even for  $n_{\text{ext}} \ll n_{\text{ext,crit}}$ , but that the maximum velocity of the shell at  $R_{UV}$  will not be much smaller than the estimates above as long as  $n_{\text{ext}}$  is not greater than  $n_{\text{ext,crit}}$ .

As an example, the dashed line in Figure 1 shows the evolution of a  $1 M_{\odot}$  shell driven into a constant density medium with  $n_{\text{ext}} = 5 \text{ cm}^{-3}$ . Of course, the circumstellar medium around a massive star in outburst is likely to have a complex density structure with a wind-blown bubble, but equations (34) and (35) show that the density must be very high to slow the shell on scales much smaller than  $R_{UV}$ .

Similar examples of a shell interacting with a medium, but in the galactic case, are shown by the dashed and dotted lines in Figure 2. The short dashed lines show shells with  $f_{\text{sh}} = 0.1$  and  $f_{\text{sh}} = 1.0$  models (eq. 30), but including a surrounding constant density medium of  $n_{\text{ext}} = 10^{-4} \text{ cm}^{-3}$  as motivated by the hot halo models of Maller & Bullock (2004). Both models attain high velocities because  $n_{\text{ext}} < n_{\text{ext,crit}}$ , but then decelerate as they accumulate more mass, effectively stopping after  $10^8 \text{ yr}$  of evolution.

<sup>3</sup> For the purposes of this estimate we include  $v_w$  in the wind mass profile, but neglect the bulk flow of the wind matter in the momentum equation in calculating  $\dot{M}_{\text{crit}}$ .

In an isothermal potential, these shells fall back again, particularly since the radiation pressure driving is not likely to be strong for timescales much larger  $10^7 - 10^8 \text{ yr}$ . For the models shown,  $L$  is held constant in time.

The dotted line in Figure 2 shows the evolution of the  $f_{\text{sh}} = 1$  model with a constant density external medium, but also with an isothermal sphere gas reservoir of the form in equation (32). For  $f_g = 0.01$ , the maximum velocity of the shell is significantly decreased, as predicted from equation (33) and for  $f_g = 0.1$  the velocity of the shell only reaches  $\sim 300 \text{ km s}^{-1}$ .

Note that in integrating the evolution of these shells we have had to make an assumption about the dust content per unit mass of the swept up material, adjusting the UV and IR opacities accordingly. We have adopted a simple parameterization by assuming that the dust-to-gas ratio of the swept up material is a constant, normalized to the Milky Way value:

$$\xi = f_{\text{dg,swept}}/f_{\text{dg,MW}}. \quad (36)$$

We adjust the UV and IR opacities by averaging  $\xi$  over the total mass of the shell, as it sweeps up ambient gas:

$$\langle \xi \rangle = \int \xi(M_{\text{sh}}) dM_{\text{sh}} / \int dM_{\text{sh}}. \quad (37)$$

All the models in black in Figure 2 that interact with an ambient medium assume  $\xi = 0.1$ , but the results are not qualitatively different if we assume the swept up medium is completely dust-less,  $\xi = 0$ . As an example, for  $f_{\text{sh}} = 1$ ,  $f_g = 0.1$ , and  $n_{\text{ext}} = 10^{-4} \text{ cm}^{-3}$  (long dashed lines) we show models for  $\xi = 0$  and  $\xi = 1$  in gray. The other models shown are not as strongly effected by this change in  $\xi$ .

In addition to the calculations presented in Figure 2, we have done a number of tests with a more realistic NFW dark matter potential. Because the density profile is steeper on large scales, the shells launched in the NFW potential generally attain higher asymptotic velocity than those launched in a singular isothermal sphere, all else being equal. However, it is clear from Figure 2 that the dynamics of shells is dominated by the large-scale gas distribution, and not the large scale potential. The maximum velocity of a shell, its velocity profile, and its long-term evolution depend sensitively on both the radial dependence of the ambient density profile and its normalization. For this reason, we have opted to focus on the simpler isothermal case, for which some analytic estimates are easily made.

## 2.4 Clouds

In the results presented above and below, we focus on the limit of a geometrically thin shell that subtends  $4\pi$  for simplicity. For clouds that cover only a small fraction of the solid angle from the source, the dynamics change quantitatively and qualitatively because a new timescale enters the problem: the cloud expansion time  $t_{\text{exp}} = (d \ln R_c / dt)^{-1}$ , where  $R_c$  is the cloud radius. In the shell limit, the timescale for the shell to change its optical depth  $\tau$  is directly coupled to the dynamical timescale because  $\tau \propto r^{-2}$ , and this determines  $R_{UV}$ , which in turn determines the asymptotic velocity. For a cloud,  $\tau \propto R_c^{-2}$  and the radius at which it becomes optically-thin to the UV is instead governed by the cloud's internal sound speed  $c_s$  and the amount by which the cloud is over- or under-pressured with respect to the background medium. Cloud

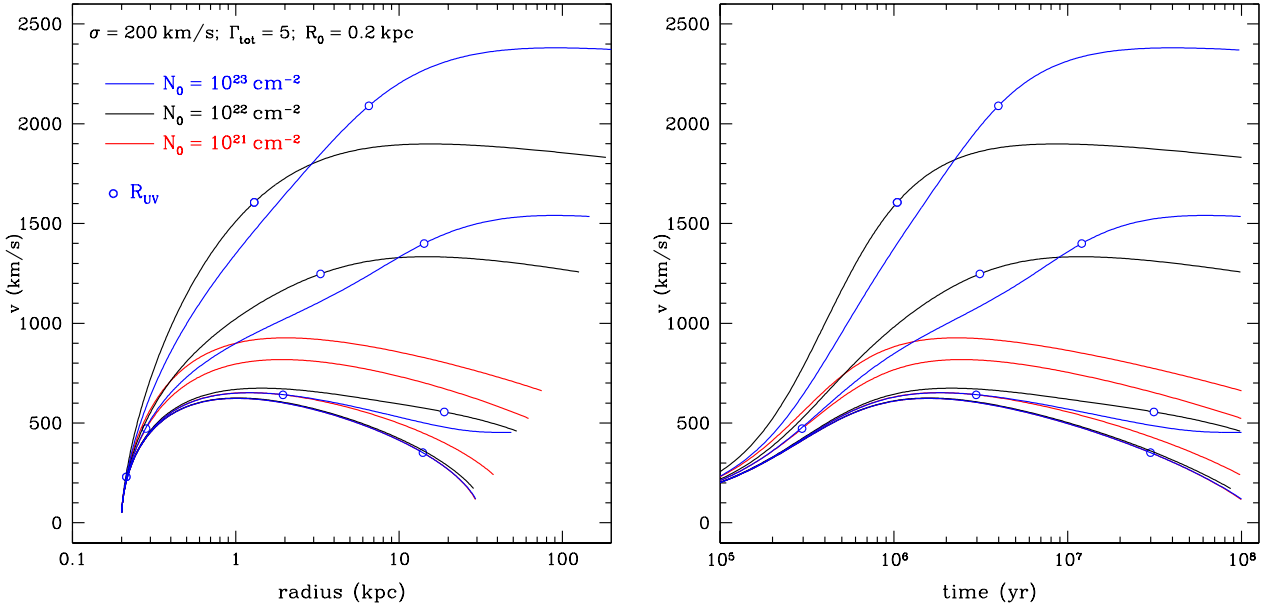


**Figure 3.** Velocity as a function of radius (left panel) and time (right panel) for dusty clouds with column densities  $N_0 = 10^{21}$  (red lines),  $10^{22}$  (black lines), and  $10^{23} \text{ cm}^{-2}$  (blue lines), expanding into vacuum with internal sound speed  $c_s = 0.1, 1, 10$ , and  $30 \text{ km s}^{-1}$  (lowest to highest for each  $N_0$ ) in an isothermal potential with  $\sigma = 200 \text{ km s}^{-1}$ . All clouds start from a launch radius of  $R_0 = 0.2 \text{ kpc}$ , have initial cloud radius of  $10 \text{ pc}$ , outward velocity of  $50 \text{ km/s}$ , and  $\Gamma_{\text{tot}} = 5$  (eqs. 38 & 40). At fixed  $\Gamma_{\text{tot}}$ , the total luminosities are different for each initial cloud column density. They are  $L \simeq 2.2 \times 10^{13}$ ,  $3.8 \times 10^{12}$ , and  $5.0 \times 10^{11} L_\odot$  for  $N_0 = 10^{23}, 10^{22}$ , and  $10^{21} \text{ cm}^{-2}$ , respectively. The blue circles denote the radius  $R_{\text{UV}}$  where the UV optical depth of the cloud drops to unity.

acceleration by radiation pressure on dust has been discussed in models of galactic winds by Murray et al. (2005, 2011).

The set of equations governing the dynamics of a radiation pressure accelerated cloud expanding into vacuum (no background medium) is

$$\frac{d}{dt}(M_c v_c) = -\frac{GMM_c}{r^2} + (1 + \min[1, \tau_{\text{IR}}] - e^{-\tau_{\text{UV}}}) \frac{L}{c} \left( \frac{A_c}{4\pi r^2} \right) \quad (38)$$

and

$$\frac{dR_c}{dt} = c_s, \quad (39)$$

where we assume a geometrically thin “pancake” geometry for the cloud,  $M_c$  is the cloud mass,  $A_c = \pi R_c^2$ ,  $\tau_{\text{UV,IR}} = M_c \kappa_{\text{UV,IR}} / A_c$ , and we limit the  $\tau_{\text{IR}}$  force terms such that even if  $\tau_{\text{IR}} \gg 1$  the cloud does not feel an enhanced force. In reality, this term will depend on the distribution of clouds in the system since the optical depth for the cloud ensemble may be much larger or smaller than unity, and may be much different than the individual cloud optical depth.

Setting the momentum equation equal to zero, we derive the generalized Eddington limit for clouds:

$$L_{\text{Edd}} = \frac{4\pi G M c}{(1 + \min[1, \tau_{\text{IR}}] - e^{-\tau_{\text{UV}}}) (A_c / M_c)}. \quad (40)$$

Note that the denominator varies from  $\simeq 2A_c/M_c$  (the single-scattering limit) as the cloud column density goes to infinity, to  $\kappa_{\text{UV}}$  ( $L_{\text{Edd}} = 4\pi G M c / \kappa_{\text{UV}}$ ) as the cloud column goes to zero. The former limit is different than the shell geometry because of the  $\tau_{\text{IR}}$  term. In the shell case, the Eddington luminosity approaches a

constant ( $L_{\text{Edd}} = 4\pi G M c / \kappa_{\text{IR}}$ ), whereas in the cloud case  $L_{\text{Edd}}$  continues to increase with increasing cloud column since we impose the condition that  $\tau_{\text{IR}}$  cannot be larger than unity.

There are additional important similarities and differences between the dynamics of shells and clouds we wish to highlight. As in the case of shells, we see that if  $L \gtrsim L_{\text{Edd}}$  and if the cloud starts optically-thick to the incoming radiation and expands as a function of radius (e.g.,  $R_c \sim t c_s$ ), because the cloud column decreases as a function of time, the cloud becomes increasingly super-Eddington as  $r$  increases, like a sail continuously unfurling in the wind. This has two consequences. First, because a small perturbation in the radial direction causes the cloud to expand and the Eddington luminosity to drop, clouds are dynamically unstable to expulsion in the single-scattering limit, as discussed for shells in Section 2.1. Second, the asymptotic velocity can be very large, as in the case of shells treated throughout this work. The simplest way to see this is to note that if  $R_c \propto r$ , then the ratio  $A_c/r^2 = \text{constant}$  on the right hand side of equation (38) and the solution for the cloud dynamics reduces to the shell case worked out in Section 2.1. However, in general  $R_c$  is not a power-law in  $r$  and this prevents a simple analytic treatment.

In the opposite limit where the cloud does not expand or simply has a very long expansion timescale relative to the dynamical timescale  $r/v$ , then  $A_c/M_c$ ,  $\tau_{\text{UV}}$ , and  $\tau_{\text{IR}}$  are effectively constant, and the solid angle subtended by the cloud decreases as  $r^{-2}$  as the cloud is driven outward. The asymptotic velocity of the cloud in the point-mass limit is then simply  $v_\infty = v_{\text{esc}}(R_0) (\Gamma - 1)^{1/2}$ , where  $\Gamma$  is the initial value of  $L/L_{\text{Edd}}$  (in eq. 40).

These limits are illustrated in Figure 3. We show velocity as a function of radius and time for radiation pressure accelerated



clouds with  $\Gamma_{\text{tot}} = L/L_{\text{Edd}} = 5$  (eq. 40), with initial column densities of  $N_0 = 10^{21}$  (red),  $10^{22}$  (black), and  $10^{23} \text{ cm}^{-2}$  (blue), expanding into vacuum with a range of internal sound speeds from  $c_s = 0.1 - 30 \text{ km/s}$  (lowest to highest) in an isothermal potential. All clouds start with the same radius of 10 pc. As expected, for small  $c_s$ , all clouds have approximately the same velocity profile, regardless of their initial column density, and their maximum velocity is  $\sim 2\sigma(L/L_{\text{Edd}} - 1)^{1/2}$  (with a modification for the extended gravitational potential). However, for higher cloud expansion speeds, the velocity evolution changes significantly, with much higher velocities attained, and depends on the initial column density of the cloud.

The fastest expanding, lowest column density cloud (highest red line) reaches only  $\sim 800 \text{ km s}^{-1}$  because the cloud rapidly becomes optically-thin to the UV radiation, because it does not have a large value of  $L/L_{\text{Edd}}$  at  $R_{\text{UV}}$ , and because it does not undergo a long-lived phase in the single-scattering limit. In contrast, the most rapidly expanding higher column clouds reach much higher velocities (highest blue and black lines). The radius (or time) at which these clouds become optically-thin to the UV is indicated by the blue circled dots, as in earlier Figures, and shows both that the extended single-scattering phase is important and the value of  $L/L_{\text{Edd}}$  at  $R_{\text{UV}}$ .

All else being equal, clouds that start with cloud radius smaller than the 10 pc value used in Figure 3 reach higher velocities because the cloud expansion timescale is shorter. For the  $N_0 = 10^{22} \text{ cm}^{-2}$  clouds, for example, if the cloud starts with a radius of 1 pc and  $c_s = 10 \text{ km s}^{-1}$ , the cloud reaches an outward velocity  $\sim 2500 \text{ km s}^{-1}$  instead of the  $\sim 1300 \text{ km s}^{-1}$  shown in Figure 3. In this regime of rapid expansion the cloud becomes optically-thin to the UV radiation on small scales and the effective Eddington ratio at  $R_{\text{UV}}$  is large, leading to a higher value of the asymptotic velocity. In this example, for a cloud that is optically-thin to the UV near  $R_0$ , the effective Eddington ratio would be  $\sim 80$  instead of 5. The rapid expansion thus allows for high acceleration in the super-Eddington flux from the source.

Note that we have assumed that there is no surrounding medium and that the clouds are not destroyed by the Kelvin-Helmholtz instability or evaporation (see, e.g., Cooper et al. 2009). We have further assumed a single constant internal sound speed and that the UV light from the central source is unobscured. In fact, we expect clouds with a range of column densities to be driven out of the system with a spread of asymptotic velocities (see Thompson & Krumholz 2014) and for the ensemble of clouds to partially obscure the central source, thereby limiting the acceleration. In addition, there is ample evidence for a hot gas component in galactic winds that the cold clouds will sweep up and interact with, potentially leading to their destruction and a different radial evolution than indicated by equation (39) (Strickland & Stevens 2000; Strickland & Heckman 2009; Zhang et al. 2014, 2015). These effects require further study.

### 3 DISCUSSION

Below, we provide brief discussions of the total momentum in radiation pressure driven flows, the applicability of our results to observations of fast outflows observed in emission and absorption in local and high-redshift galaxies and AGN, prescriptions for outflows in large-scale cosmological simulations, and the implications

of our results for star cluster disruption and massive star eruptions. We focus on shells throughout instead of clouds since the dynamics of the latter require a more complete understanding of how the dynamics change when an ensemble of clouds of different column densities, radii, and velocities obscure the central source. This important problem will be the focus of a future investigation.

#### 3.1 The Asymptotic Momentum of Shells

A key diagnostic of observed outflows in galaxies and AGN is the momentum ratio

$$\zeta = \frac{\dot{M}v}{(L/c)} = \frac{M_{\text{sh}}v}{(L/c)(r/v)}, \quad (41)$$

where the first equality is applicable to a continuous wind with mass loss rate  $\dot{M}$ , and the second equality is applicable to a shell. These two definitions are equivalent since, typically, one measures the column density in blue-shifted absorption features (such as the resonance lines of Fe, Mg, and Na) to infer

$$\dot{M} = 4\pi r N m_p v \quad \text{or} \quad M_{\text{sh}} = 4\pi r^2 N m_p, \quad (42)$$

where  $N$  is the column density of gas, so that

$$\zeta = \frac{4\pi r N m_p v}{(L/c)} \quad (43)$$

in either case. In general, one must assume a relative abundance of the tracer (e.g., Na or Mg) with respect to total gas, which usually involves an uncertain ionization correction (e.g., Murray et al. 2007).

A primary observational difference between a continuous wind and a shell would of course be in the absorption line profile, which for a perfect geometrically-thin single shell would be a delta-function in velocity along the line of sight toward a point source of radiation. However, for a shell in proximity to a finite-sized source (a star or galaxy), the observed absorption line would be broadened geometrically by the projection of the moving shell onto the source.

The momentum ratio  $\zeta$  is important because for  $\zeta \gg 1$ , either (1) the shell or wind had very high effective  $\tau_{\text{IR}}$  (e.g., Murray et al. 2010), or (2) the shell was initially energy-driven, as in the early evolution of a supernova remnant. Since the radial scale of the absorbing material is in general not known, absorption line studies determine  $\zeta$  with significant uncertainties. Emission-line studies with molecular emission, [CII], or in the optical/UV (e.g., H $\alpha$ , [NII]) provide a complementary view of winds, and in some cases find evidence for  $\zeta > 1$  (e.g., Ciccone et al. 2014; Genzel et al. 2011; Section 3.2).

The momentum ratio in the case of a single shell of fixed mass, observed at a radius  $r \gtrsim R_{\text{UV}}$ , can be approximated by

$$\zeta = \frac{M_{\text{sh}}v_{\text{UV}}^2}{rL/c} \simeq 2f(\tau_0) \left( \frac{\Gamma_{\text{SS}}}{\Gamma_{\text{tot}}} \right) \left( \frac{R_{\text{UV}}}{r} \right), \quad (44)$$

where  $f(\tau_0) = (1 + \tau_{\text{IR}} - e^{-\tau_{\text{UV}}})$  evaluated at the launch radius  $R_0$ . For  $\tau_{\text{UV}} > 1$ , but  $\tau_{\text{IR}} < 1$ ,  $\Gamma_{\text{SS}} \simeq \Gamma_{\text{tot}}$  and  $f(\tau_0) \sim 1$ , implying that  $\zeta$  should always be of order unity or smaller, since for  $r > R_{\text{UV}}$ ,  $\zeta$  rapidly decreases. This behavior can be seen in both the  $f_{\text{sh}} = 0.1$  and the  $f_{\text{sh}} = 1$  models shown by the solid lines in Figure 4 (left), which shows  $\zeta(r)$ . All models have  $\zeta \sim 0.1$  on 10 – 100 kpc scales. Note that even though the shells accelerate beyond  $R_{\text{UV}}$ , the measured momentum decreases, because

in this regime  $v^2(r)/r$  decreases. Models that sweep up mass decelerate, and  $\zeta(r)$  decreases more rapidly. In the single-scattering limit of  $\tau_{UV} > 1$ , but  $\tau_{IR} < 1$  at  $R_0$ , one would simply estimate  $v_{UV}^2 \sim R_{UV}L/M_{sh}c$  by dimensional analysis of the momentum equation, and then substituting into equation (44), one again finds that  $\zeta(R_{UV}) \simeq 1$ .

Since the two key observables for characterizing shell-like outflows are velocity and column density, and since these enter the calculation of  $\zeta$  directly, in the right panel of Figure 4 we show  $M_{sh}/4\pi r^2 m_p$  versus  $v$  for the same models as in the left panel, and in both panels of Figure 2. Note that, as expected, the momentum ratio reaches  $\sim 1$  for the shells dominated by the single-scattering term and then decreases on larger scales, where the shell spends the most time. If radiation pressure driven shells are a good model for fast outflows,  $\zeta < 1$  should be observed in some systems. More discussion is provided in Section 3.2.

If the effective IR optical depth of the shell is much larger than unity at the launch point (see Section 3.7 below for caveats), then  $f(\tau_0) \sim \tau_{IR}(R_0)$ ,  $\Gamma_{tot} \sim \Gamma_{IR}$  and  $\zeta(r)$  can be significantly increased. For the  $f_{sh} = 1$  example in Figures 2 and 4,  $\tau_{IR}(R_0) \simeq 8$  and  $\zeta(r)$  peaks at  $\simeq 2$  on the scale of a few times  $R_0$ . For higher  $\tau_{IR}(R_0)$  one finds higher values of  $\zeta$  on the scale of  $R_{IR}$ . In particular, when  $\tau_{IR}(R_0) \gg 1$  and  $\Gamma_{IR} \gg 1$ , one finds that at  $R_{IR}$

$$\begin{aligned} \zeta(R_{IR}) &= \frac{M_{sh}v_{IR}^2}{R_{IR}L/c} \simeq 2 \frac{R_{IR}}{R_0} \\ &\simeq 5.8 \kappa_{IR,0.7}^{1/2} M_{sh,9}^{1/2} R_{0,0.1kpc}^{-1}. \end{aligned} \quad (45)$$

Note that while  $\zeta(R_{IR})$  is not proportional to  $\tau_{IR}(R_0)$ , the maximum value of  $\zeta$  (see Fig. 4), which occurs on scales smaller than  $R_{IR}$ , is proportional to  $\tau_{IR}(R_0)$  (for fixed  $\Gamma_{IR} \gg 1$ ). The red solid lines in Figure 4 show  $\zeta(r)$  and  $N(v)$  for a model with  $f_{sh} = 5$  so that  $\tau_{IR}(R_0) \simeq 40$ . The peak in  $\zeta(r)$  occurs at a few times  $R_0$  and is about 4 times lower than  $\tau_{IR}(R_0)$ . See Section 3.7 for a discussion of some of the uncertainties associated with high- $\tau_{IR}$  solutions in the context of radiation pressure driven shells.

### 3.2 Fast Outflows from Rapidly Star-Forming Galaxies, Starbursts, & Post-Starbursts

**Fast Outflows in Emission:** Cicone et al. (2014) have recently presented data on a collection of AGN and star-formation dominated systems with outflows seen in molecular emission. We show  $\zeta$  as a function of  $L_{bol}$  and a histogram of  $\zeta$  for their sample in the panels of Figure 5. Red, blue, and green denote AGN fractions of  $L_{AGN}/L_{bol} > 0.5$ ,  $0.2 \leq L_{AGN}/L_{bol} \leq 0.5$ , and  $L_{AGN}/L_{bol} < 0.2$ , respectively, for the systems with outflows detected at high significance.<sup>4</sup>

If interpreted as shells accelerated by radiation pressure on dust we find that the systems with  $\zeta \lesssim 2 - 3$  are readily explained, given their bolometric luminosities. For example, Mrk 273 and 231, have  $L_{AGN}/L_{bol} \simeq 0.08$  and  $\simeq 0.3$ ,  $L_{bol} \simeq 1.7 \times 10^{12}$  and  $4 \times 10^{12} L_\odot$ , and total outflow mass of  $\sim 10^{8.2}$  and  $\sim 10^{8.4} M_\odot$ , respectively, on scales of  $\simeq 0.6$  kpc, with average velocities of

$\simeq 600 - 700 \text{ km s}^{-1}$ . These parameters are all in the range expected for relatively low-mass shells accelerated by radiation pressure, with dynamics similar to the  $f_{sh} = 0.1$  model shown in Figures 2 and 4.

Systems with high values of  $\zeta$  in the Cicone et al. (2014) compilation likely require large initial values of  $\tau_{IR}(R_0)$  (see red line in Figure 4; Sections 3.1 and 3.7). Another possibility is that a fairly rapid decrease in the AGN or starburst luminosity could imply large  $\zeta$  even though the dynamics is consistent with radiation pressure acceleration in the single-scattering limit. Future explorations could employ the shell models described here and/or continuous wind models to constrain  $R_0$  and the source of driving with the data on  $\zeta$ . A careful comparison with the observed dynamics could be used to quantitatively test the radiation pressure driven shell picture discussed here.

**Fast Outflows in Absorption:** Tremonti et al. (2007) and Diamond-Stanic et al. (2012) report the discovery of fast  $\gtrsim 1000 \text{ km s}^{-1}$  outflows in starburst and post-starburst galaxies. In particular, Diamond-Stanic et al. (2012) show that the system J0905+5759 has strongly blue-shifted Mg II absorption with a shell-like velocity profile centered at  $-2470 \text{ km s}^{-1}$  (ranging from  $\simeq -3000$  to  $-2200 \text{ km s}^{-1}$ ), covering the entire galaxy. The effective radius of the galaxy is  $\simeq 100 \text{ pc}$ , with stellar mass of  $10^{10.7} M_\odot$ , velocity dispersion of  $\simeq 250 \text{ km s}^{-1}$ , and total IR luminosity of  $10^{12.6} L_\odot$  (Diamond-Stanic, private communication; see also Sell et al. 2014; Geach et al. 2014).

Repeating the calculation shown in the left panel of Figure 2, but for  $\sigma = 250 \text{ km s}^{-1}$ ,  $R_0 = 100 \text{ pc}$ , and  $\Gamma_{tot} = 2.5$  ( $L_{bol} \simeq 1.1 \times 10^{13} L_\odot$ ) we find  $v_{UV} \simeq 1900 \text{ km s}^{-1}$  and  $v_\infty \simeq 2500 \text{ km s}^{-1}$  for  $f_{sh} = 0.05$  ( $M_{sh} \simeq 1.5 \times 10^8 M_\odot$ ). If interpreted as a shell accelerated by the continuum radiation pressure on dust grains, the shell would have a radial scale of  $\gtrsim 1.6 \text{ kpc}$ , which is consistent with the observed blue continuum.

We note that although the velocity and shell mass calculated are roughly consistent with the observational constraints, the required bolometric luminosity of the system is somewhat high compared to the observations. However, there are many factors that complicate straightforward modeling of this system. In particular, a realistic model for the luminosity of the system as a function of time and the large-scale gravitational potential change the velocity profile quantitatively. More importantly, though, as highlighted in Figure 2, the surrounding medium swept up by the shell can qualitatively effect its dynamics. In this context, it is again worth noting that the Eddington ratio for dusty shells is linearly dependent on the gas-to-dust-ratio: larger dust content per gram of gas lowers the critical luminosity for shell expulsion. Finally, the absorption line profile for this system has significant width in velocity (Diamond-Stanic et al. 2012), which may indicate that the cloud picture discussed in Section 2.4 is more applicable than the case of a simple shell. Future work should model the system with an ensemble of absorbing clouds accelerated to a range of velocities (see Fig. 3) to see if the observations can be reproduced.

**The Local Starburst M82:** M82 has an extensively studied outflow, with evidence for  $\sim 200 - 600 \text{ km s}^{-1}$  line-emitting gas and dust on kpc scales, a molecular outflow on small scales, and hot nuclear X-ray emission (e.g., Shopbell & Bland-Hawthorn 1998; Walter et al. 2002; Strickland & Heckman 2009).

Using the dust-scattered UV emission from the central starburst (Hoopes et al. 2005), Coker et al. (2013) calculated the Ed-

<sup>4</sup> By assuming a uniform medium, Cicone et al. (2014) overestimate  $\zeta$  by a factor of 3, which we have corrected in Figure 5. We also adopt the lowest values of the total inferred outflowing gas mass in their tables. In some cases  $\zeta$  could be larger by a factor of  $\sim 3$ .

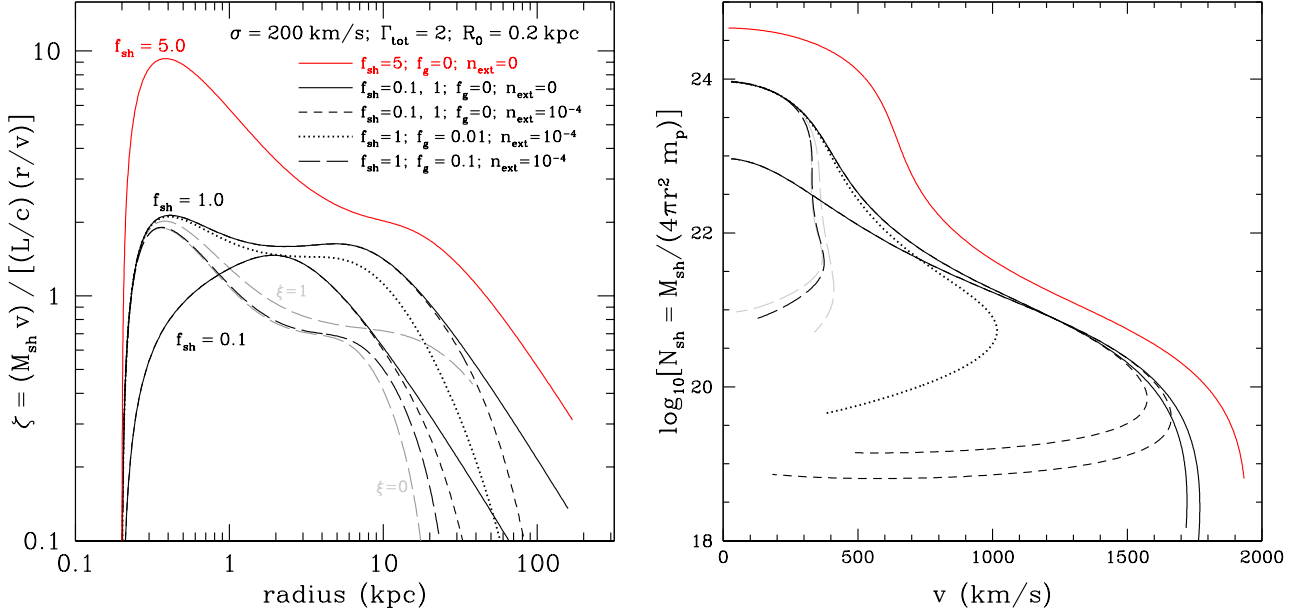


**Figure 4.** (Left): Momentum ratio  $\zeta$  (eq. 41) as a function of radius for the shells shown in Figure 2, but with an additional high- $\zeta$  model for illustration with  $f_{\text{sh}} = 5$  (red line), which has  $\tau_{\text{IR}}(R_0) \simeq 40$ . (Right): Total hydrogen column density of shells as a function of velocity. Models and linestyles are the same as in the left panel and Figure 2.

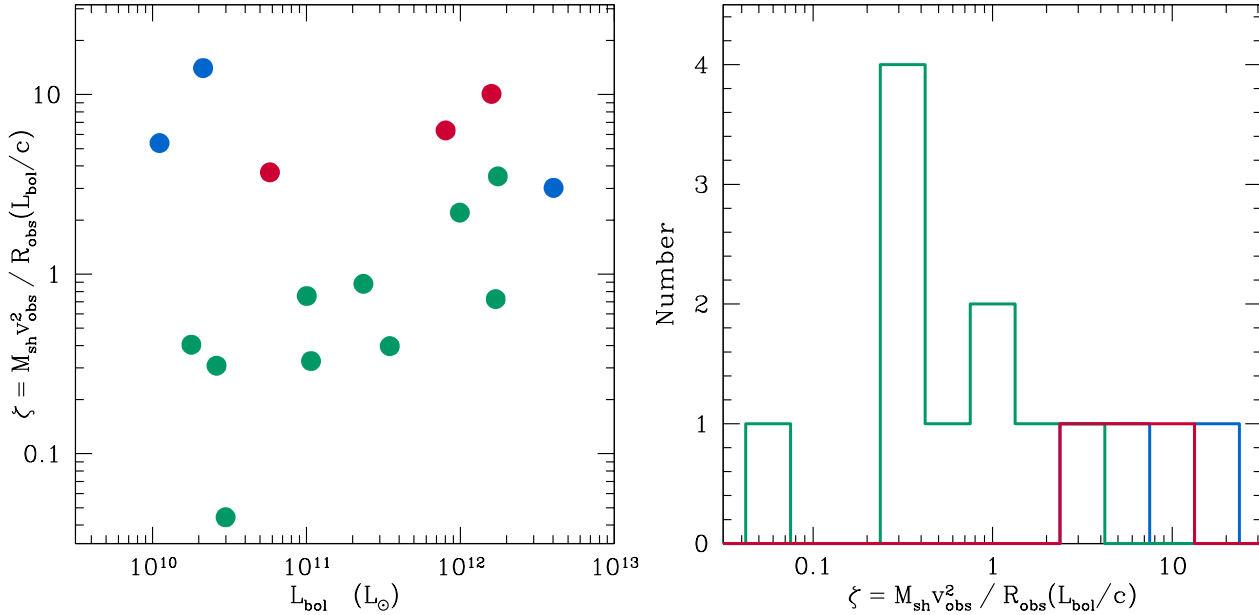


**Figure 5.** (Left): Observed momentum ratio from a sample of AGN and starburst galaxies as a function of bolometric luminosity (Cicone et al. 2014). Red, blue, and green points show systems where the central AGN luminosity  $L_{\text{AGN}}/L_{\text{bol}} > 0.5$ ,  $0.2 \leq L_{\text{AGN}}/L_{\text{bol}} \leq 0.5$ , and  $L_{\text{AGN}}/L_{\text{bol}} < 0.2$ , respectively. (Right): Histogram of momentum ratios from the same sample. A CO-to- $\text{H}_2$  conversion factor of 0.8 has been used for calculating  $M_{\text{sh}}$ .

dington ratio for dusty gas on 0.5 – 5 kpc scales. Using the large-scale rotation curve from Greco et al. (2012), Coker et al. (2013) found that although significantly more UV escapes the starburst along the minor axis than along our line of sight, the Eddington ratio is still much less than unity on large scales. These results imply that a shell-like radiation pressure-driven outflow cannot account for the dusty gas currently seen on kpc scales. Moreover,

this result highlights the fact that the additional large-scale acceleration that produces the high velocities discussed here may not be generic, but may only occur in special circumstances or geometries. One mitigating factor is that Förster Schreiber et al. (2003) find that the bolometric luminosity of the M82 starburst was a factor of  $\sim 4$  larger 6 Myr ago, indicating that the system may have potentially approached the single-scattering Eddington limit on scales

within the starburst<sup>5</sup>, and would have certainly exceeded  $\Gamma_{UV} = 1$  (eq. 12).

### 3.3 Broad Absorption Line Quasars & Ultra-Fast Outflows

Some BAL quasars have detached potentially shell-like absorption profiles with blueshifted velocities of  $\simeq 4000 - 5000 \text{ km s}^{-1}$ . Some have velocities over  $20,000 \text{ km s}^{-1}$  (e.g., Pounds et al. 2003; Tombesi et al. 2010; Gupta et al. 2013).

Taking  $L_{AGN} = 10^{47} \text{ ergs s}^{-1}$  and  $R_0 = R_{\text{sub}} \simeq 2 \text{ pc}$  and  $M_{\text{sh}} = 10^5, 10^6$ , and  $10^7 M_{\odot}$ , we find  $v_{\infty} \simeq 2.8 \times 10^4, 1.7 \times 10^4$  and  $1.1 \times 10^4 \text{ km s}^{-1}$ , respectively, for Milky Way gas-to-dust ratio. Such high velocity outflows might emerge along the line of sight to Type-I quasars in a very short timescale  $\ll 10^6 \text{ yr}$  (see eq. 21) and become optically-thin to the UV emission from the quasar on scales  $< 0.1 - 1 \text{ kpc}$  (see eq. 6). These types of dusty shells are related to the suggestion by Scoville & Norman (1995) that dusty material near quasars could be accelerated to  $\sim 0.1 c$ .

### 3.4 Previous Work & Prescriptions for Cosmological Simulations

Murray et al. (2005) discussed galactic winds driven by the combined momentum input of radiation pressure on dust and supernovae and wrote down the momentum equation for a shell in an isothermal potential, as in equation (22). The primary difference between their results and our work here is in the assumed distribution of mass swept up by the outflowing shell. In particular, they assumed an isothermal mass distribution for the gas so that  $M_{\text{sh}} \propto r$  (as in eq. 32). In this case, in the single-scattering limit,

$$v \frac{dv}{dr} = -\frac{\sigma^2}{r} + \frac{L}{c} \frac{G}{2\sigma^2 f_g r} \quad (46)$$

where  $f_g = M_{\text{sh}}/M$  is a constant at each radius. Note that for constant  $f_g$ , both the gravitational acceleration and the radiation pressure acceleration have the same radial dependence. This is why the fairly large enhancement in the asymptotic velocity of a shell launched by radiation pressure we emphasize here was not noted in that work. The long dashed line in the panels of Figure 2 assumes an isothermal sphere for the surrounding gas distribution and shows a shell model that closely tracks the expectation from equation (46) and Murray et al. (2005).

Several studies of the enrichment of the intergalactic medium have used the so-called "momentum scalings" (radiation pressure or supernovae) based on the work of Murray et al. (2005) (e.g., Oppenheimer & Davé 2006, 2008). Typically, these are that

$$v_{\infty} \simeq \text{few} \times \sigma \quad (47)$$

and that<sup>6</sup>

$$\dot{M}/\text{SFR} \propto \sigma^{-1} \quad (48)$$

These same scalings and variants have also been tested in models of the mass-metallicity relation by Peeples & Shankar (2011).

<sup>5</sup>  $\Gamma_{\text{SS}} \sim 1$  for  $M(r < 300 \text{ pc}) = 10^9 M_{\odot}$ ,  $M_{\text{sh}} = 10^8 M_{\odot}$ ,  $R = 300 \text{ pc}$  and  $L = 2 \times 10^{11} L_{\odot}$  (see eq. 11).

<sup>6</sup> This follows from equating  $L/c \simeq \epsilon \text{SFR} c \sim \dot{M} v_{\infty}$  for a star-forming galaxy in the single-scattering limit (Murray et al. 2005).

Our work suggests prescriptions that would more accurately capture the physics of radiation pressure driven shells, as opposed to continuous winds. The simplest is that the "few" in equation (47) could in some cases be as large as  $\sim 10$ , depending on the geometry of the outflow and the surrounding medium, a potentially important factor that should be taken into account and explored in more detail. Second, the Eddington luminosity for a shell is given simply by equation (23), which can be thought of as three different Eddington luminosities in three different regimes. If the shell is (1) optically-thick to the IR, (2) optically-thin to the IR, but optically-thick to the UV, or (3) optically-thin to the UV, the Eddington luminosity is given by equations (10), (11), and (12), respectively, depending on the surface density of the shell. If  $L \geq L_{\text{Edd}}$  in the appropriate limit, then the ISM is ejected. Note that in general  $L_{\text{Edd}}$  is dust-to-gas ratio dependent and thus metallicity dependent.

The dynamics of the shell and its interaction with the surrounding circumgalactic medium could be calculated from equation (6), either via a subgrid model in large-scale cosmological simulations, or explicitly in high-resolution simulations of individual galaxies. Such a prescription for large-scale simulations would differ qualitatively from what is currently done in that a large fraction of the ISM would be ejected in single events, fallback would be determined predominantly by the circumgalactic medium density profile, and the velocity of the material could approach  $\sim 10 \times \sigma$  along lines of sight with little gas (see eq. 28). In this picture, the ratio  $\dot{M}/\text{SFR}$  should instead be thought of as the ratio of the total mass ejected to the total mass formed between each star formation and ejection event, where the timescale between ejections would be determined by the gas accretion rate from the IGM and from re-accreted (formerly ejected) gas. Ejection episodes and fallback might precipitate radiative cooling of the hot circumgalactic medium, as in the work of Fraternali & Binney 2008 (see also Marasco et al. 2012; Fraternali et al. 2013).

### 3.5 Star Cluster Disruption

The estimates made here can also effect giant molecular cloud (GMC) disruption. Murray et al. (2010) discussed the acceleration of GMC gas by radiation pressure and other forces (see also Krumholz & Matzner 2009), and Murray et al. (2011) provide a general description of launching these shells and clouds from star clusters to velocities high enough to escape the host galaxy and generate supershells. In these works, analytic estimates for the critical star cluster stellar mass required to generate extra-planar gas was estimated, based on the assumption that  $v_{\infty}$  for such a shell would be of order a few times the cluster escape velocity. If the self-gravity of the shell dominates the total gravitational force, and if the central star cluster reaches the single-scattering Eddington limit ( $\Gamma_{\text{SS}} \simeq 1$ ), then we have shown here that  $v_{\infty} \simeq (2GM_{\text{sh}}/R_0)^{1/2} (R_{\text{UV}}/R_0)^{1/2} \simeq 200 \text{ km/s } M_{\text{sh},6}^{3/4} \kappa_{\text{UV},3}^{1/4} (5 \text{ pc}/R_0)^{-1}$ , implying that large-scale super-shells from GMC disruption could be driven high above the plane of a large galaxy by massive star clusters with total stellar mass significantly less than  $10^6 M_{\odot}$ . Faster asymptotic velocities are more easily obtained in a shell-like geometry.

Because shell formation during GMC disruption by radiation pressure may be generic (Yeh & Matzner 2012), our results are important for diagnosing the dynamics of observed systems like 30 Doradus (Lopez et al. 2011; Pellegrini et al. 2011).



### 3.6 Massive Star Eruptions

Figure 1 shows that shells from massive star outbursts can be accelerated to velocities much larger than the escape velocity at the dust formation radius. Here, we briefly discuss applications to the outbursts of Luminous Blue Variables and the shells observed around the yellow hypergiants VY CMa and IRC 10420.

Eta Carinae's homunculus shows a number of different kinematic components. The primary mass reservoir is  $\sim 10 M_\odot$  with a velocity of  $\simeq 500 \text{ km s}^{-1}$  (Smith et al. 2003; Smith 2006). There is also a faster component at  $\sim 1000 - 2000 \text{ km s}^{-1}$  and a much faster, but much less massive component moving at  $\sim 3000 - 6000 \text{ km s}^{-1}$  (Smith 2008). All are associated with the Great Eruption approximately 170 years ago in which Eta Car reached an estimated bolometric luminosity of  $\sim 2 \times 10^7 L_\odot$  (Davidson & Humphreys 1997).

In this context it is worth asking if radiation pressure on dust grains could have dominated the acceleration of any of the kinematic components. Examining Figure 1 and equations (19) and (21), this possibility appears unlikely for the more massive component because (1) the asymptotic velocity would only be  $\sim 250 - 350 \text{ km s}^{-1}$  (allowing for some uncertainty in  $L$ ) and (2) the timescale to reach this velocity is too long,  $\sim 10^3 \text{ yr}$ . For the less massive high velocity components radiation pressure on dust might have had more of a role, depending on their mass. Although not shown in Figure 1, calculations with  $L = 10^7 L_\odot$  and  $M_{\text{sh}} = 10^{-2}, 10^{-3} M_\odot$ , and  $10^{-4} M_\odot$  reach  $v_\infty \simeq 970, \simeq 1650$ , and  $\simeq 2650 \text{ km s}^{-1}$  on decade-to-year timescales (eq. 21).<sup>7</sup>

Clearly only small amounts of mass can be accelerated to the requisite velocities on short timescales. That these components might be dynamically accelerated by radiation pressure on dust is connected to treatments of line-driven photon-tired outflows in this context by Owocki et al. (2004). It is worth noting that the maximum possible velocity for a dusty shell accelerated from the dust formation/destruction radius is

$$v_\infty \simeq \left( \frac{4L \kappa_{\text{UV}}^2 \sigma_{\text{SB}} T_{\text{sub}}^4}{\pi c^2} \right)^{1/4} \sim 3500 \text{ km s}^{-1} L_7^{1/4} \kappa_{\text{UV},3}^{1/2} T_{1500} \quad (49)$$

for a shell that starts optically-thin to the incident UV radiation from the star and a nominal Milky Way gas-to-dust ratio (compare with eq. 19). Allowing for a factor of 2 higher luminosity and dust-to-gas ratio boosts  $v_\infty$  to  $\sim 4200 \text{ km s}^{-1}$ .

The much lower velocity dusty outflows of the yellow hypergiants VY CMa and IRC 10420 are also of interest. The latter has  $L \simeq 5 \times 10^5 L_\odot$  and a mass of  $\sim 10 - 20 M_\odot$ , with dusty shells observed at velocity  $\sim 40 \text{ km s}^{-1}$  on  $\sim 10^3 \text{ AU}$  scales, with equivalent mass loss rates of  $\sim 10^{-4} - 10^{-3} M_\odot \text{ yr}^{-1}$  (Oudmaijer et al. 1996; Humphreys et al. 1997, 2002; Dinh-V.-Trung et al. 2009). The observed velocity is large compared to the escape velocity at the dust formation radius,  $\sim 20 \text{ km s}^{-1}$  and the typical velocities of dusty AGB star winds. The observed parameters for VY CMa

<sup>7</sup> The photospheric temperature of Eta Carinae and the yellow hypergiants discussed here is lower than needed for significant UV emission. For this reason,  $\kappa_{\text{UV}}$  used throughout this work should be replaced by the flux-mean dust opacity for a  $\sim 5000 - 7000 \text{ K}$  blackbody: e.g.,  $\kappa \simeq 100 - 300 \text{ cm}^2 \text{ g}^{-1}$ . This lowers the expected asymptotic velocity according to the scalings in equations (19) and (49).

are similar. It has a prominent dusty arc with velocity  $\sim 50 \text{ km s}^{-1}$  on  $10^3 \text{ AU}$  scales, but with both slower ( $\sim 10 \text{ km s}^{-1}$ ) and faster ( $\sim 100 - 200 \text{ km s}^{-1}$ ) material observed smaller and larger scales, respectively (Monnier et al. 1999; Humphreys et al. 2005; Muller et al. 2007).

In accord with equations (19) and (21), low-mass shells with  $M_{\text{sh}} = 0.1 M_\odot$  from a star with  $L = 5 \times 10^5 L_\odot$ , and  $M = 15 M_\odot$  can be accelerated to  $\sim 50 - 75 \text{ km s}^{-1}$  on scales of  $\sim 10 - 100 \text{ AU}$ , but reach an asymptotic velocity of  $\sim 150 \text{ km s}^{-1}$  at  $\sim 10^4 \text{ AU}$ . Higher mass shells of  $\sim 1 - 3 M_\odot$  reach only  $v_\infty \simeq 100 \text{ km s}^{-1}$ .<sup>8</sup> Here, as throughout this paper, we assume that the shell subtends  $4\pi$  and that it sees the central source throughout its acceleration to  $v_\infty$ . Both assumptions should be called into question for these mass ejection episodes since the dusty nebulae are observed to be asymmetric and since multiple shells exist for both stars. Even so, the large-scale acceleration that is the focus of this paper might be required to explain the  $\sim 100 - 200 \text{ km s}^{-1}$  material seen around VY CMa by Humphreys et al. (2005) (their Fig. 13).

### 3.7 Uncertainties & Assumptions

**Geometry & Emergent Radiation Field:** We assume a simple geometry throughout most of this paper: a point source with a surrounding spherical shell, or a cloud that subtends much less than  $4\pi$  and expands at its internal sound speed. In most contexts, a shell is unlikely to subtend  $4\pi$  and may break up into discrete clouds and the clouds may be subject to destruction by hydrodynamical processes if there is a background medium. Perhaps more importantly, in the case of galactic-scale winds, the set of sources is not point-like, although the galaxy may be represented by a distribution of actively star-forming and disrupting star clusters.

In addition, we have assumed that the UV continuum escapes from the source to large scales and that it is time-steady. In the galaxy context, the central source may be obscured by the ISM of the galaxy, or by intervening shells of material, or many expanding clouds at different velocities and column densities (Thompson & Krumholz 2014).<sup>9</sup> Although we have shown that the acceleration time is short with respect to the characteristic time for a stellar population to change luminosity (eq. 21), the time evolution could be important effect for the long-term dynamics in galactic potentials ( $> 10^7 - 10^8 \text{ yr}$ ). Similar to the discussion presented in Zhang & Thompson (2012) it is worth noting that strong blue-shifted absorption can be observed in post-starburst galaxies because the timescale for material driven to  $\sim 100 \text{ kpc}$  is longer than  $\simeq 10^8 \text{ yr}$ . It is worth emphasizing that the momentum ratio  $\zeta$  (eq. 41) would then be overestimated. The time-dependence of

<sup>8</sup> Note that these models have shell masses only marginally below the critical photon tiring limit discussed in footnote 2. For  $M_{\text{sh}} = 3 M_\odot$  and  $L = 5 \times 10^5 L_\odot$ , one finds that  $Lt/(M_{\text{sh}} v^2/2) \sim 4$  on  $100 \text{ AU}$  scales. A lower  $L$ , or a larger dust condensation temperature ( $T_{\text{sub}} = 1500 \text{ K}$ ) than assumed here would put these models into the photon tiring limit (Owocki & Gayley 1997).

<sup>9</sup> A related point is that throughout this work we have implicitly neglected the importance of ionizing photons, which carry approximately as much momentum as the UV continuum in the single-scattering limit. If the medium between the source and the shell was optically-thin to ionizing photons, the dynamics of the shells would change since these photons would couple to the shell until it reached a very low column density.

a quasar might produce analogous effects; a fast outflow could be seen on large scales around a (now) less luminous AGN and a correspondingly low value of  $\zeta$  would be inferred.

**Large  $\tau_{\text{IR}}$ :** Using 2D planar gray flux-limited diffusion (FLD) with a realistic dust opacity Krumholz & Thompson (2013) showed that the asymptotic momentum of shells driven with initially very large  $\tau_{\text{IR}}$  is not proportional to  $\tau_{\text{IR}}$ . In particular, for an initial mid-plane optical depth  $\tau_{\text{IR}} \simeq 100 - 1000$  and IR Eddington ratio of  $\infty$  (gravitational acceleration of zero), they find that the asymptotic momentum taken up by the ejected material is only  $\simeq 1 - 10$  times that expected from the single-scattering limit. This result follows from the strong density-flux anti-correlation that develops as a result of channels which open in the 2D flow due in part to the radiation-driven Rayleigh-Taylor instability.

Recent results from Davis et al. (2014) using a more sophisticated and accurate radiation transport algorithm (the Variable Eddington Tensor [VET] method; Davis et al. 2012; Jiang et al. 2012) supersede these earlier calculations, and produce different results than FLD (see Krumholz & Thompson 2012). In particular, Davis et al. (2014) find a less extreme flux-density anticorrelation that produces more net momentum coupling between the radiation and the dusty gas relative to FLD. This leads to a qualitatively different outcome in some simulations: Krumholz & Thompson (2012) find steady radiation pressure-driven convection whereas (Davis et al. 2014) find an unbound outflow for the same initial conditions.

These results are important and should be more fully studied. There is yet no systematic study of the momentum coupling in super-Eddington dusty outflows with a large range of initial IR optical depths using multi-dimensional VET calculations.<sup>10</sup> Such a study will be crucial in understanding the viability of radiation pressure in generating outflows with  $\zeta \gg 1$  in a range of contexts. As implied by Figure 1 and the discussion in Section 3.6, outbursts from massive stars will in general have large initial  $\tau_{\text{IR}}$  if dust forms. In addition, we expect large average IR optical depths for massive star clusters and ULIRGs, and in the dusty pc-scale environments around AGN. If radiation pressure is a viable mechanism for the dynamics of these outflows then large effective IR optical depths for momentum coupling may be required by the data in some systems (e.g., Fig. 5). These results from observational and numerical works may ultimately point either to other sources of wind driving, such as energy-driven flows powered by supernovae (e.g., Chevalier & Clegg 1985; Strickland & Stevens 2000; Strickland & Heckman 2009; but, see Zhang et al. 2014), or additional momentum input by supernovae (e.g., Murray et al. 2005; Thompson et al. 2005; Faucher-Giguère et al. 2013), cosmic-rays (e.g., Jubelgas et al. 2008; Socrates et al. 2008; Hanasz et al. 2013), magneto-centrifugal acceleration, or other processes.

**Grain Physics :** We have simplified a number of issues associated with grain physics. First, we have neglected the temperature dependence of the Rosseland-mean opacity of dust grains in the optically-thick limit, relevant when  $\tau_{\text{IR}} > 1$  (Pollack et al. 1994; Semenov et al. 2003). In particular,  $\kappa_R(T) \simeq 2.4(T/100 \text{ K})^2 \text{ cm}^2/\text{g}$  for  $T \lesssim 150 \text{ K}$  and  $\kappa_R(T) \sim \text{const}$  for  $150 \lesssim T \lesssim 1500 \text{ K}$  for Milky Way gas-to-dust ratio. Second,

we have assumed that the gas and dust grains are completely dynamically coupled. In reality, the momentum coupling between dust and gas is grain size dependent, and will depend both on the charge distribution and magnetic field strengths in the medium being accelerated (Draine & Salpeter 1979b). Third, in the models presented throughout this paper, we assume that the grains in the gas are not destroyed by either the hard radiation fields of a central AGN or starburst, by grain-gas collisions, or sputtering (see, e.g., Draine & Salpeter 1979a; Draine & Salpeter 1979b; Voit 1991; Draine 1981, 1995). All of these issues deserve further investigation in the context of dusty radiation pressure accelerated shells.

## 4 SUMMARY

We have shown that the typical expectation for radiation pressure driven flows that  $v_\infty \sim v_{\text{esc}}$  at the launch radius  $R_0$  is not correct for dusty shells and expanding clouds. In these cases, the single-scattering phase of acceleration can dominate the dynamics. For the shell case, the asymptotic velocity scales as  $v_\infty \sim (R_{\text{UV}}L/M_{\text{sh}}c)^{1/2} \propto \kappa_{\text{UV}}^{1/4}(L/M_{\text{sh}})^{1/2}$ . As discussed in Section 1 and 2 this result is equivalent to  $v_\infty \sim v_{\text{esc}}\Gamma^{1/2}$  evaluated at the point where the shell becomes optically-thin to the UV,  $R_{\text{UV}}$ . For clouds, the dynamics is more complicated. For individual rapidly expanding clouds (see Fig. 3), high velocities can be readily achieved, either through a long-lived single-scattering phase of acceleration, or because they become optically-thin to the UV radiation very rapidly so that they see a highly super-Eddington flux. The basic result  $v_\infty$  can be very large has implications for the dynamics of dusty shells in a number of contexts, including giant molecular cloud disruption around forming star clusters, outbursts from massive stars, galactic winds driven by star formation, and fast dusty outflows driven by AGN. In particular, it appears possible to accommodate the surprising result from Diamond-Stanic et al. (2012) that post-starburst galaxies with velocity dispersions of order  $\sim 200 - 250 \text{ km s}^{-1}$  can drive shell-like outflows with velocity of  $\sim 2000 \text{ km s}^{-1}$  even though the Eddington ratio at the launch radius was only  $\Gamma_{\text{tot}} \sim 1$ .

## ACKNOWLEDGMENTS

The authors thank the anonymous referee for a timely and thoughtful report. TAT is supported in part by NASA Grant NNX10AD01G. TAT thanks Aleks Diamond-Stanic, Nathan Smith, David Weinberg, Smita Mathur, and Dong Zhang for useful conversations and Chris Kochanek for a critical reading of the text. EQ is supported in part by NASA ATP Grant 12-ATP12-0183.

## REFERENCES

- Abbott, D. C. 1978, *ApJ*, 225, 893
- Andrews, B. H., & Thompson, T. A. 2011, *ApJ*, 727, 97
- Bond, H. E., Bedin, L. R., Bonanos, A. Z., et al. 2009, *ApJ*, 695, L154
- Chevalier, R. A., & Clegg, A. W. 1985, *Nature*, 317, 44
- Chiao, R. Y., & Wickramasinghe, N. C. 1972, *MNRAS*, 159, 361
- Cicone, C., Maiolino, R., Sturm, E., et al. 2014, *A&A*, 562, A21

<sup>10</sup> The related issue of the acceleration of individual clouds with dust opacity and accurate radiation hydrodynamics remains to be investigated (see Proga et al. 2014).

- Coker, C. T., Thompson, T. A., & Martini, P. 2013, *ApJ*, 778, 79
- Cooper, J. L., Bicknell, G. V., Sutherland, R. S., & Bland-Hawthorn, J. 2009, *ApJ*, 703, 330
- Davidson, K., & Humphreys, R. M. 1997, *ARA&A*, 35, 1
- Davis, S. W., Jiang, Y.-F., Stone, J. M., & Murray, N. 2014, *arXiv:1403.1874*
- Davis, S. W., Stone, J. M., & Jiang, Y.-F. 2012, *ApJS*, 199, 9
- Diamond-Stanic, A. M., Moustakas, J., Tremonti, C. A., et al. 2012, *ApJ*, 755, L26
- Dijkstra, M., & Loeb, A. 2009, *MNRAS*, 396, 377
- Dijkstra, M., & Loeb, A. 2008, *MNRAS*, 391, 457
- Dinh-V-Trung, Muller, S., Lim, J., Kwok, S., & Muthu, C. 2009, *ApJ*, 697, 409
- Draine, B. T., & Salpeter, E. E. 1979, *ApJ*, 231, 77
- Draine, B. T., & Salpeter, E. E. 1979, *ApJ*, 231, 438
- Draine, B. T. 1981, *ApJ*, 245, 880
- Draine, B. T. 1995, *Ap&SS*, 233, 111
- Fabian, A. C. 1999, *MNRAS*, 308, L39
- Faucher-Giguère, C.-A., Quataert, E., & Hopkins, P. F. 2013, *MNRAS*, 433, 1970
- Ferrara, A., Aiello, S., Ferrini, F., & Barsella, B. 1990, *A&A*, 240, 259
- Ferrara, A. 1993, *ApJ*, 407, 157
- Förster Schreiber, N. M., Genzel, R., Lutz, D., & Sternberg, A. 2003, *ApJ*, 599, 193
- Geach, J. E., Hickox, R. C., Diamond-Stanic, A. M., et al. 2014, *Nature*, 516, 68
- Genzel, R., Newman, S., Jones, T., et al. 2011, *ApJ*, 733, 101
- Gillett, F. C., Backman, D. E., Beichman, C., & Neugebauer, G. 1986, *ApJ*, 310, 842
- Greco, J. P., Martini, P., & Thompson, T. A. 2012, *ApJ*, 757, 24
- Gupta, A., Mathur, S., Krongold, Y., & Nicastro, F. 2013, *ApJ*, 772, 66
- Hanasz, M., Lesch, H., Naab, T., et al. 2013, *ApJ*, 777, L38
- Harwit, M. 1962, *ApJ*, 136, 832
- Hoopes, C. G., Heckman, T. M., Strickland, D. K., et al. 2005, *ApJ*, 619, L99
- Hopkins, P. F., Quataert, E., & Murray, N. 2011, *MNRAS*, 417, 950
- Hopkins, P. F., Quataert, E., & Murray, N. 2012, *MNRAS*, 421, 3488
- Hopkins, P. F., Quataert, E., & Murray, N. 2012, *MNRAS*, 421, 3522
- Humphreys, R. M., Smith, N., Davidson, K., et al. 1997, *AJ*, 114, 2778
- Humphreys, R. M., Davidson, K., & Smith, N. 2002, *AJ*, 124, 1026
- Humphreys, R. M., Davidson, K., Ruch, G., & Wallerstein, G. 2005, *AJ*, 129, 492
- Ivezic, Z., & Elitzur, M. 1995, *ApJ*, 445, 415
- Ivezic, Z., & Elitzur, M. 1997, *MNRAS*, 287, 799
- Jiang, Y.-F., Stone, J. M., & Davis, S. W. 2012, *ApJS*, 199, 14
- Jubelgas, M., Springel, V., Enßlin, T., & Pfrommer, C. 2008, *A&A*, 481, 33
- King, A. 2003, *ApJ*, 596, L27
- King, A. 2005, *ApJ*, 635, L121
- Kochanek, C. S. 2011, *ApJ*, 741, 37
- Kochanek, C. S. 2011, *ApJ*, 743, 73
- Kochanek, C. S., Szczygieł, D. M., & Stanek, K. Z. 2012, *ApJ*, 758, 142
- Krumholz, M. R., & Matzner, C. D. 2009, *ApJ*, 703, 1352
- Krumholz, M. R., & Thompson, T. A. 2007, *ApJ*, 669, 289
- Krumholz, M. R., & Thompson, T. A. 2012, *ApJ*, 760, 155
- Krumholz, M. R., & Thompson, T. A. 2013, *MNRAS*, 434, 2329
- Lopez, L. A., Krumholz, M. R., Bolatto, A. D., Prochaska, J. X., & Ramirez-Ruiz, E. 2011, *ApJ*, 731, 91
- Maller, A. H., & Bullock, J. S. 2004, *MNRAS*, 355, 694
- Miller, A. A., Smith, N., Li, W., et al. 2010, *AJ*, 139, 2218
- Monnier, J. D., Tuthill, P. G., Lopez, B., et al. 1999, *ApJ*, 512, 351
- Muller, S., Dinh-V-Trung, Lim, J., et al. 2007, *ApJ*, 656, 1109
- Murray, N., Quataert, E., & Thompson, T. A. 2005, *ApJ*, 618, 569
- Murray, N., Martin, C. L., Quataert, E., & Thompson, T. A. 2007, *ApJ*, 660, 211
- Murray, N., Quataert, E., & Thompson, T. A. 2010, *ApJ*, 709, 191
- Murray, N., Ménard, B., & Thompson, T. A. 2011, *ApJ*, 735, 66
- O'dell, C. R., York, D. G., & Henize, K. G. 1967, *ApJ*, 150, 835
- Oppenheimer, B. D., & Davé, R. 2006, *MNRAS*, 373, 1265
- Oppenheimer, B. D., & Davé, R. 2008, *MNRAS*, 387, 577
- Ostriker, E. C., & Shetty, R. 2011, *ApJ*, 731, 41
- Oudmaijer, R. D., Groenewegen, M. A. T., Matthews, H. E., Blommaert, J. A. D. L., & Sahu, K. C. 1996, *MNRAS*, 280, 1062
- Owocki, S. P., & Gayley, K. G. 1997, *Luminous Blue Variables: Massive Stars in Transition*, 120, 121
- Owocki, S. P., Gayley, K. G., & Shaviv, N. J. 2004, *ApJ*, 616, 525
- Pellegrini, E. W., Baldwin, J. A., & Ferland, G. J. 2011, *ApJ*, 738, 34
- Peeples, M. S., & Shankar, F. 2011, *MNRAS*, 417, 2962
- Pollack, J. B., Hollenbach, D., Beckwith, S., et al. 1994, *ApJ*, 421, 615
- Pounds, K. A., Reeves, J. N., King, A. R., et al. 2003, *MNRAS*, 345, 705
- Prieto, J. L., Kistler, M. D., Thompson, T. A., et al. 2008, *ApJ*, 681, L9
- Prieto, J. L., Sellgren, K., Thompson, T. A., & Kochanek, C. S. 2009, *ApJ*, 705, 1425
- Proga, D., Jiang, Y.-F., Davis, S. W., Stone, J. M., & Smith, D. 2014, *ApJ*, 780, 51
- Ridgway, S. T., Joyce, R. R., Connors, D., Pipher, J. L., & Dainty, C. 1986, *ApJ*, 302, 662
- Roth, N., Kasen, D., Hopkins, P. F., & Quataert, E. 2012, *ApJ*, 759, 36
- Salpeter, E. E. 1974, *ApJ*, 193, 585
- Scoville, N., & Norman, C. 1995, *ApJ*, 451, 510
- Scoville, N. 2003, *Journal of Korean Astronomical Society*, 36, 167
- Scoville, N. Z., Polletta, M., Ewald, S., Stolovy, S. R., Thompson, R., & Rieke, M. 2001, *AJ*, 122, 3017
- Sell, P. H., Tremonti, C. A., Hickox, R. C., et al. 2014, *arXiv:1404.0677*
- Semenov, D., Henning, T., Helling, C., Ilgner, M., & Sedlmayr, E. 2003, *A&A*, 410, 611
- Shopbell, P. L., & Bland-Hawthorn, J. 1998, *ApJ*, 493, 129
- Socrates, A., Davis, S. W., & Ramirez-Ruiz, E. 2008, *ApJ*, 687, 202
- Smith, N., & Gehrz, R. D. 1998, *AJ*, 116, 823
- Smith, N., Gehrz, R. D., Hinz, P. M., et al. 2003, *AJ*, 125, 1458
- Smith, N. 2005, *MNRAS*, 357, 1330
- Smith, N. 2006, *ApJ*, 644, 1151
- Smith, N. 2008, *Nature*, 455, 201
- Smith, N. 2013, *MNRAS*, 429, 2366
- Strickland, D. K., & Stevens, I. R. 2000, *MNRAS*, 314, 511
- Strickland, D. K., & Heckman, T. M. 2009, *ApJ*, 697, 2030
- Thompson, T. A., Quataert, E., & Murray, N. 2005, *ApJ*, 630, 167

- Thompson, T. A., Prieto, J. L., Stanek, K. Z., et al. 2009, *ApJ*, 705, 1364
- Thompson, T. A., & Krumholz, M. R. 2014, arXiv:1411.1769
- Tombesi, F., Cappi, M., Reeves, J. N., et al. 2010, *A&A*, 521, A57
- Tremonti, C. A., Moustakas, J., & Diamond-Stanic, A. M. 2007, *ApJ*, 663, L77
- Voit, G. M. 1991, *ApJ*, 379, 122
- Walter, F., Weiss, A., & Scoville, N. 2002, *ApJ*, 580, L21
- Yeh, S. C. C., & Matzner, C. D. 2012, *ApJ*, 757, 108
- Zhang, D., & Thompson, T. A. 2012, *MNRAS*, 424, 1170
- Zhang, D., Thompson, T. A., Murray, N., & Quataert, E. 2014, *ApJ*, 784, 93
- Zhang, D., Thompson, T. A., Murray, N., & Quataert, E. 2015, in preparation